

Classification and Geometry of General Perceptual Manifolds

SueYeon Chung^{1,2}, Daniel D. Lee^{2,3}, and Haim Sompolinsky^{2,4,5}

¹*Program in Applied Physics, School of Engineering and Applied Sciences,
Harvard University, Cambridge, MA 02138, USA*

²*Center for Brain Science, Harvard University, Cambridge, MA 02138, USA*

³*School of Engineering and Applied Science, University of Pennsylvania, Philadelphia, PA 19104, USA*

⁴*Racah Institute of Physics, Hebrew University, Jerusalem 91904, Israel*

⁵*Edmond and Lily Safra Center for Brain Sciences, Hebrew University, Jerusalem 91904, Israel*

Perceptual manifolds arise when a neural population responds to an ensemble of sensory signals associated with different physical features (e.g., orientation, pose, scale, location, and intensity) of the same perceptual object. Object recognition and discrimination requires classifying the manifolds in a manner that is insensitive to variability within a manifold. How neuronal systems give rise to invariant object classification and recognition is a fundamental problem in brain theory as well as in machine learning. Here we study the ability of a readout network to classify objects from their perceptual manifold representations. We develop a statistical mechanical theory for the linear classification of manifolds with arbitrary geometry revealing a remarkable relation to the mathematics of conic decomposition. Novel geometrical measures of *manifold radius* and *manifold dimension* are introduced which can explain the classification capacity for manifolds of various geometries. The general theory is demonstrated on a number of representative manifolds, including ℓ_2 ellipsoids prototypical of strictly convex manifolds, ℓ_1 balls representing polytopes consisting of finite sample points, and orientation manifolds which arise from neurons tuned to respond to a continuous angle variable, such as object orientation. The effects of label sparsity on the classification capacity of general manifolds are elucidated, revealing a universal scaling relation between label sparsity and the manifold radius. Theoretical predictions are corroborated by numerical simulations using recently developed algorithms to compute maximum margin solutions for manifold dichotomies. Our theory and its extensions provide a powerful and rich framework for applying statistical mechanics of linear classification to data arising from neuronal responses to object stimuli, as well as to artificial deep networks trained for object recognition tasks.

PACS numbers: 87.18.Sn, 87.19.lv, 42.66.Si, 07.05.Mh

I. INTRODUCTION

A fundamental cognitive task performed by animals and humans is the invariant perception of objects, requiring the nervous system to discriminate between different objects despite substantial variability in each object's physical features. For example, in vision, the mammalian brain is able to recognize objects despite variations in their orientation, position, pose, lighting and background. Such impressive robustness to physical changes is not limited to vision; other examples include speech processing which requires the detection of phonemes despite variability in the acoustic signals associated with individual phonemes; and the discrimination of odors in the presence of variability in odor concentrations. Sensory systems are organized as hierarchies consisting of multiple layers transforming sensory signals into a sequence of distinct neural representations. Studies of high level sensory systems, e.g., the inferotemporal cortex (IT) in vision [1], auditory cortex in audition [2], and piriform cortex in olfaction [3], reveal that even the late sensory stages exhibit significant sensitivity of neuronal responses to physical variables. This suggests that sensory hierarchies generate representations of objects that although not entirely invariant to changes in physical features, are still readily decoded by a down-

stream system. This hypothesis is formalized by the notion of the untangling of perceptual manifolds [4–6]. This viewpoint underlies a number of studies of object recognition in deep neural networks for artificial intelligence [7–10].

To conceptualize perceptual manifolds, consider a set of N neurons responding to a specific sensory signal associated with an object as shown in Fig. 1. The neural population response to that stimulus is a vector in \mathbb{R}^N . Changes in the physical parameters of the input stimulus that do not change the object identity modulate the neural state vector. The set of all state vectors corresponding to responses to all possible stimuli associated with the same object can be viewed as a manifold in the neural state space. In this geometrical perspective, object recognition is equivalent to the task of discriminating manifolds of different objects from each other. Presumably, as signals propagate from one processing stage to the next in the sensory hierarchy, the geometry of the manifolds is reformatted so that they become “untangled,” namely they are more easily separated by a biologically plausible decoder [1]. In this paper, we model the decoder as a simple single layer network (the perceptron) and ask how the geometrical properties of the perceptual manifolds influence their ability to be separated by a linear classifier.

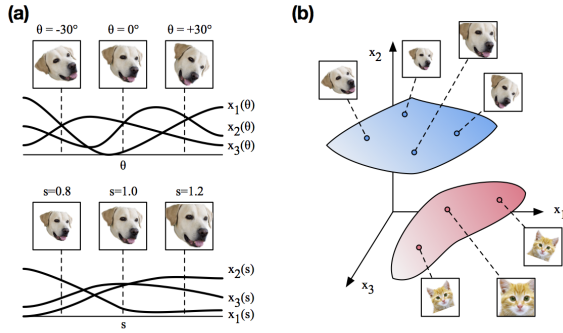


Figure 1. Perceptual manifolds in neural state space. (a) Firing rates of neurons responding to images of a dog shown at various orientations θ and scales s . The response to a particular orientation and scale can be characterized by an N -dimensional population response. (b) The population responses to the images of the dog form a continuous manifold representing the complete set of invariances in the \mathbb{R}^N neural activity space. Other object images, such as those corresponding to a cat in various poses, are represented by another manifold in this vector space.

The issue of quantifying linear separability has previously been studied in the context of the classification of points, by a perceptron, using combinatorics [11] and statistical mechanics [12, 13]. Gardner’s statistical mechanics theory is extremely important as it provides accurate estimates of the perceptron capacity beyond function counting by incorporating robustness measures. The robustness of a linear classifier is quantified by the margin, which measures the distance between the separating hyperplane and the closest point. Maximizing the margin of a classifier is a critical objective in machine learning, providing Support Vector Machines (SVM) with their good generalization performance guarantees [14].

The above theories focus on separating a finite set of points with no underlying geometrical structure and are not applicable to the problem of manifold classification which deals with separating infinite number of points geometrically organized as manifolds. This paper addresses the important question of how to quantify the capacity of the perceptron for dichotomies of input patterns described by manifolds. In an earlier paper, we have presented the analysis for classification of manifolds of extremely simple geometry, namely balls [15]. However, the previous results have limited applicability as the neural manifolds arising from realistic physical variations of objects can exhibit much more complicated geometries. Can statistical mechanics deal with the classification of manifolds with complex geometry?

In this paper, we develop a theory of linear classification of general manifolds, formalized in Sec. II. The theory is exact in the thermodynamic limit where the dimension of the manifolds is finite while both the number of neu-

rons in the representation and the number of manifolds grow to infinity. Extending Gardner’s approach we solve the mean field equations of the replica theory (Sec. III) and employ the Karush-Kuhn-Tucker conditions for convex quadratic optimization to delineate the qualitative and quantitative consequences of the mean field theory. This theory enables not only the evaluation of the capacity but also the support structure of the solution that maximizes the margin, extending the theory of SVMs for the classification of a finite number of random vectors to general manifolds. In addition to the study of the classification capacity, we introduce (Sec. IV) novel geometrical measures of manifolds which are motivated by the mean field theory; in particular, we provide new definitions of manifold dimension and radius, denoted as D_M and R_M , respectively. Interestingly, we show (Sec. V) that in the limit of high dimensional manifolds, these quantities are sufficient for estimating the classification capacity. We demonstrate the general theory in several prototypical examples for different classes of data: strictly convex manifolds such as ℓ_2 ellipsoids (Sec. VI), polytopes represented by ℓ_1 balls (Sec. VII), and smooth but non-convex manifolds such as orientation manifolds (Sec. VIII). Another important issue is the effect of sparsity in the labels, which arise in many biological and computational contexts. For a finite set of uncorrelated points, it is well known that a significant imbalance in the binary labels increases the classification capacity. Here we study (Sec. IX) the effect of label sparsity on manifold classification and analyze the rich consequences of the interaction between manifold size, dimension and class sparsity.

Our theory extends the statistical mechanics of linear classifications to complex realistic data structures and serves as a basis for further developments in this field. At the same time, our analysis reveals surprisingly rich connections between the manifold replica theory and other mathematical domains, including the theory of conic decompositions, high dimensional statistics of convex bodies, and the properties of trigonometric moment curves. Finally, our results are summarized and discussed in Sec. X.

II. MODEL OF MANIFOLDS

Manifolds in affine subspaces: We model a set of P perceptual manifolds corresponding to P perceptual object. Each manifold M^μ for $\mu = 1, \dots, P$ consists of a compact subset of an affine subspace of \mathbb{R}^N with *affine dimension* D with $D < N$. A point on the manifold $\mathbf{x}^\mu \in M^\mu$ can be parameterized as:

$$\mathbf{x}^\mu(\vec{s}) = \sum_{i=1}^{D+1} s_i \mathbf{u}_i^\mu, \quad (1)$$

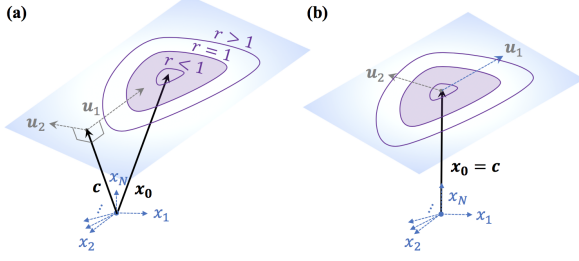


Figure 2. Model of manifolds in affine subspaces. (a) $D = 2$ manifold embedded in \mathbb{R}^N . \mathbf{c} is the orthogonal translation vector for the affine space and \mathbf{x}_0 is the center of the manifold. As the scale r is varied, the manifold shrinks to the point \mathbf{x}_0 , or expands to fill the entire affine space. (b) Centered manifold where the orthogonal translation vector \mathbf{c} and center \mathbf{x}_0 coincide.

where the \mathbf{u}_i^μ are a set of orthonormal bases of the $(D+1)$ -dimensional linear subspace containing M^μ . The $D+1$ components s_i represents the coordinates of the manifold point within this subspace and are constrained to be in the set $\vec{s} \in \mathcal{S}$. The bold notation for \mathbf{x}^μ and \mathbf{u}_i^μ indicates they are vectors in \mathbb{R}^N whereas the arrow notation for \vec{s} indicates it is a vector in \mathbb{R}^{D+1} . The set \mathcal{S} defines the shape of the manifolds and encapsulates the affine constraint. For simplicity, we will first assume the manifolds have the same geometry so that the coordinate set \mathcal{S} is the same for all the manifolds; extensions that consider heterogeneous geometries are provided in Sec. III D.

We study the separability of P manifolds into two classes, denoted by binary labels $y^\mu = \pm 1$, by a linear hyperplane passing through the origin. A hyperplane is described by a weight vector $\mathbf{w} \in \mathbb{R}^N$, normalized so $\|\mathbf{w}\|^2 = N$ and the hyperplane correctly separates the manifolds with a margin $\kappa \geq 0$ if it satisfies,

$$y^\mu \mathbf{w} \cdot \mathbf{x}^\mu \geq \kappa \quad (2)$$

for all μ and $\mathbf{x}^\mu \in M^\mu$. Since linear separability is a convex problem, separating the manifolds is equivalent to separating the convex hulls, $\text{conv}(M^\mu) = \{\mathbf{x}^\mu(\vec{s}) \mid \vec{s} \in \text{conv}(\mathcal{S})\}$, where

$$\text{conv}(\mathcal{S}) = \left\{ \sum_{i=1}^{D+1} \alpha_i \vec{s}_i \mid \vec{s}_i \in \mathcal{S}, \alpha_i \geq 0, \sum_{i=1}^{D+1} \alpha_i = 1 \right\}. \quad (3)$$

The position of an affine subspace relative to the origin can be defined via the translation vector that is closest to the origin. This *orthogonal translation vector* \mathbf{c}^μ is perpendicular to all the affine displacement vectors in M^μ . Equivalently, all the points in the affine subspace have equal projections on \mathbf{c}^μ , i.e., $\vec{\mathbf{x}}^\mu \cdot \mathbf{c}^\mu = \|\mathbf{c}^\mu\|$ for all $\mathbf{x}^\mu \in M^\mu$ (Fig. 2(a)).

We will assume that the norms of all the translation vectors are the same, denoted by $\|\mathbf{c}^\mu\| = c$. It is convenient

to represent the translational vectors in terms of their coordinates in the $D+1$ subspaces. We will denote this representation by the $D+1$ dimensional vector \vec{c} , common to all the manifolds, such that $\vec{s} \cdot \vec{c} = c^2$ for all $\vec{s} \in \mathcal{S}$. One possible choice of coordinates would be to have $\vec{c} = (0, 0, \dots, 0, c)$ and the coordinate set $\mathcal{S} = \{(s_1, s_2, \dots, s_D, c)\}$. This parameterization is convenient since it constrains the variability in the manifolds to be in the first D components of \vec{s} . However, the general theory developed below is independent of the choice of coordinates.

To investigate the separability properties of manifolds, it is helpful to consider scaling a manifold M^μ by an overall scale factor r without changing its shape. We define the scaling relative to a center $\vec{s}^0 \in \mathcal{S}$ by a scalar $r > 0$, by

$$rM^\mu = \left\{ \sum_{i=1}^{D+1} [s_i^0 + r(s_i - s_i^0)] \mathbf{u}_i^\mu \mid \vec{s} \in \mathcal{S} \right\} \quad (4)$$

When $r \rightarrow 0$, the manifold rM^μ converges to a point: $\mathbf{x}_0^\mu = \sum_i s_i^0 \mathbf{u}_i^\mu$. On the other hand, when $r \rightarrow \infty$, the manifold rM^μ spans the entire affine subspace. If the manifold has a symmetric shape (such as for an ellipsoid), there is a natural choice for a center. We will see later that our theory suggests a natural definition for the center point for general, asymmetric manifolds. In general, the translation vector \vec{c} and center \vec{s}^0 need not coincide as shown in Fig. 2(a).

Bounds on linear separability of manifolds: For dichotomies of P input points in \mathbb{R}^N at zero margin, $\kappa = 0$, the number of dichotomies that can be separated by a linear hyperplane through the origin is given by [11]:

$$C_0(P, N) = 2 \sum_{k=0}^{N-1} C_k^{P-1} \leq 2^P \quad (5)$$

where $C_k^n = \frac{n!}{k!(n-k)!}$ is the binomial coefficient for $n \geq k$, and zero otherwise. This result holds for P input vectors that obey the mild condition that the vectors are in *general position*, namely that all subsets of input vectors of size $p \leq N$ are linearly independent.

For large P and N , the probability $\frac{1}{2^P} C_0(P, N)$ of a dichotomy being linearly separable depends only upon the ratio $\frac{P}{N}$ and exhibits a sharp transition at the critical value of $\alpha_0 = 2$. Unfortunately, we are not aware of a comprehensive extension of Cover's counting theorem for general manifolds. Nevertheless, we can provide lower and upper bounds on the number of linearly realizable dichotomies by considering the limit of $r \rightarrow 0$ and $r \rightarrow \infty$ under the following general conditions.

First, in the limit of $r \rightarrow 0$, the linear separability of P manifolds becomes equivalent to the separability of the P centers. This leads to the requirement that the centers of the manifolds, \mathbf{x}_0^μ , are in general position in \mathbb{R}^N . Second, we consider the conditions under which the mani-

folds are linearly separable when $r \rightarrow \infty$ so that the manifolds span complete affine subspaces. For a weight vector \mathbf{w} to consistently assign the same label to all points on an affine subspace, it must be orthogonal to all the displacement vectors in the affine subspace. In that case, the label assigned will be the same as that assigned to the manifold's orthogonal translation vector. Hence, to realize a dichotomy of P manifolds when $r \rightarrow \infty$, the weight vector \mathbf{w} must lie in a null space of dimension $N - D_{tot}$ where D_{tot} is the rank of the union of affine displacement vectors. When the basis vectors \mathbf{u}_i^μ are in general position, then $D_{tot} = \min(DP, N)$. Then for the affine subspaces to be separable, $PD < N$ is required and the projections of the P orthogonal translation vectors need also be separable in the $N - D_{tot}$ dimensional null space. Under these general conditions, the number of dichotomies for D -dimensional affine subspaces that can be linearly separated, $C_D(P, N)$, can be related to the number of dichotomies for a finite set of points via:

$$C_D(P, N) = C_0(P, N - PD). \quad (6)$$

From this relationship, we conclude that for affine subspaces: when $\frac{P}{N} \geq \frac{1}{D}$, $C_D(P, N) = 0$; when $\frac{P}{N} \leq \frac{1}{D+1}$, $C_D(P, N) = 2^P$; and when $\frac{P}{N} = \frac{1}{D+\frac{1}{2}}$, $C_D(P, N) = 2^{P-1}$. Thus, the ability to linearly separate D -dimensional affine subspaces exhibits a transition from always being separable to never being separable at the critical ratio $\frac{P}{N} = \frac{2}{1+2D}$ for large P and N (see Supplementary Materials, SM, Sec. S1).

For general D -dimensional manifolds with finite size, the number of dichotomies that are linearly separable will be lower bounded by $C_D(P, N)$ and upper bounded by $C_0(P, N)$. We introduce the notation, $\alpha_M(\kappa)$, to denote the maximal load $\frac{P}{N}$ that allows for linear separability of randomly labeled manifolds with high probability. Therefore, from the above considerations, it follows that the critical load $\alpha_M(\kappa = 0)$ is bounded by,

$$\frac{2}{1+2D} \leq \alpha_M(\kappa = 0) \leq 2. \quad (7)$$

III. STATISTICAL MECHANICAL THEORY

In order to make theoretical progress beyond the bounds above, we need to make additional statistical assumptions about the manifold spaces and labels. Specifically, we will assume that the individual components of \mathbf{u}_i^μ are drawn independently and from identical Gaussian distributions with zero mean and variance $\frac{1}{N}$, and that the binary labels $y^\mu = \pm 1$ are randomly assigned to each manifold with equal probabilities. We will study the thermodynamic limit where $N, P \rightarrow \infty$, but with a finite load $\alpha = \frac{P}{N}$. In addition, the manifold geometries are

specified by the set \mathcal{S} in \mathbb{R}^{D+1} are held fixed in the thermodynamic limit. Under these assumptions, the bounds in Eq. (7) can be extended to the linear separability of general manifolds with finite margin κ , and characterized by the reciprocal of the critical load ratio $\alpha_M^{-1}(\kappa)$,

$$\alpha_0^{-1}(\kappa) \leq \alpha_M^{-1}(\kappa) \leq \alpha_0^{-1}(\kappa) + D \quad (8)$$

where $\alpha_0(\kappa)$ is the maximum load for separation of random i.i.d. points with a margin κ given by the Gardner theory [12],

$$\alpha_0^{-1}(\kappa) = \int_{-\kappa}^{\infty} Dt (t + \kappa)^2 \quad (9)$$

with Gaussian measure $Dt = \frac{1}{\sqrt{2\pi}} e^{-\frac{t^2}{2}}$. For many interesting cases, the affine dimension D is large and the gap in Eq. (8) is overly loose. In the following, we use the replica approach to study the classification problem for manifolds with finite sizes and evaluate the dependence of the capacity and the nature of the solution on the geometrical properties of the manifolds.

A. Mean field theory of the capacity

Following Gardner's framework [12, 13], we compute the statistical average of $\log V$, where V is the volume of the space of the solutions, which in our case can be written as:

$$V = \int d^N \mathbf{w} \delta(\|\mathbf{w}\|^2 - N) \prod_{\mu, \mathbf{x}^\mu \in M^\mu} \Theta(y^\mu \mathbf{w} \cdot \mathbf{x}^\mu - \kappa), \quad (10)$$

$\Theta(\cdot)$ is the Heaviside function to enforce the margin constraints in Eq. (2), along with the delta function to ensure $\|\mathbf{w}\|^2 = N$. In the following, we focus on the properties of the maximum margin solution, namely the solution for the largest load α_M for a fixed margin κ , or equivalently for a given α_M , the solution when the margin κ is maximized.

As shown in Appendix A, we prove that the general form of the inverse capacity, exact in the thermodynamic limit, is:

$$\alpha_M^{-1}(\kappa) = \langle F(\vec{t}) \rangle_{\vec{t}} \quad (11)$$

where

$$F(\vec{t}) = \min_{\vec{v}} \left\{ \|\vec{v} - \vec{t}\|^2 \mid \vec{v} \cdot \vec{s} + \kappa \leq 0, \forall \vec{s} \in \mathcal{S} \right\} \quad (12)$$

and $\langle \dots \rangle_{\vec{t}}$ is an average over random $D+1$ dimensional vectors \vec{t} whose components are i.i.d. normally distributed $t_i \sim \mathcal{N}(0, 1)$.

The inequality constraints in Eq. (12) can be written equivalently, as a constraint on the point on the manifold

with *maximal* projection on \vec{v} . We therefore consider the following convex function, known as the *support function* of \mathcal{S} :

$$g_{\mathcal{S}}(\vec{v}) = \max_{\vec{s} \in \mathcal{S}} \{\vec{v} \cdot \vec{s} \mid \vec{s} \in \mathcal{S}\}, \quad (13)$$

which can be used to write the constraint for $F(\vec{t})$ as

$$F(\vec{t}) = \min_{\vec{v}} \left\{ \|\vec{v} - \vec{t}\|^2 \mid g_{\mathcal{S}}(\vec{v}) + \kappa \leq 0 \right\} \quad (14)$$

The components of the Gaussian vector \vec{t} represent the quenched randomness in the solution due to the quenched variability in the manifolds' basis vectors and the labels; the difference $\vec{v} - \vec{t}$ represents the scaled variability due to the entropy of the solution space (see Appendix A). Together, these contributions comprise \vec{v} which, up to a sign, represents the fields induced by the solution \vec{w} on the basis vectors of the manifolds, \mathbf{u}_i^μ . To conform to the standard definition of convex optimizations such as Eq. (12), the components of \vec{v} are reversed with respect to these fields, hence they obey inequality constraints that appear opposite to the original constraints in Eq. (2).

Karush-Kuhn-Tucker (KKT) conditions: To gain a deeper understanding of the nature of the maximum margin solution, it is useful to consider the KKT conditions of the convex optimization in Eq. 14 [16]. For each \vec{t} , the KKT conditions that characterize the unique solution of \vec{v} for $F(\vec{t})$ is given by:

$$\vec{v} = \vec{t} - \lambda \tilde{s}(\vec{t}) \quad (15)$$

where

$$\begin{aligned} \lambda &\geq 0 \\ g_{\mathcal{S}}(\vec{v}) + \kappa &\leq 0 \\ \lambda [g_{\mathcal{S}}(\vec{v}) + \kappa] &= 0 \end{aligned} \quad (16)$$

The vector $\tilde{s}(\vec{t})$ is one of the *subgradients* of the support function at \vec{v} , $\tilde{s}(\vec{t}) \in \partial g_{\mathcal{S}}(\vec{v})$. As a subgradient, it satisfies the requirement,

$$g_{\mathcal{S}}(\vec{v}') \geq g_{\mathcal{S}}(\vec{v}) + \partial g_{\mathcal{S}}(\vec{v}) \cdot (\vec{v}' - \vec{v}) \quad (17)$$

for all vectors \vec{v}' and lies within the convex hull, $\partial g_{\mathcal{S}}(\vec{v}) \subseteq \text{conv}(\mathcal{S})$. When the support function is differentiable, the subgradient $\partial g_{\mathcal{S}}(\vec{v})$ is unique and is equivalent to the gradient of the support function: $\partial g_{\mathcal{S}}(\vec{v}) = \nabla g_{\mathcal{S}}(\vec{v})$. In this case $\tilde{s}(\vec{t})$ corresponds to the unique point obeying,

$$\tilde{s}(\vec{t}) = \nabla g_{\mathcal{S}}(\vec{v}) = \arg \max_{\vec{s} \in \mathcal{S}} \vec{v} \cdot \vec{s} \quad (18)$$

Since the support function is positively homogeneous, $g_{\mathcal{S}}(\gamma \vec{v}) = \gamma g_{\mathcal{S}}(\vec{v})$ for all $\gamma > 0$, $\partial g_{\mathcal{S}}(\vec{v}) = \partial g_{\mathcal{S}}(\hat{v})$ and

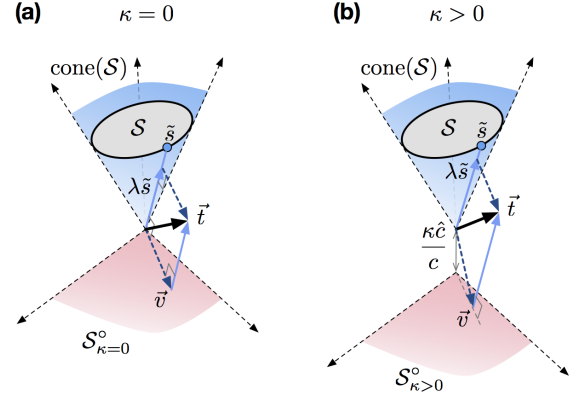


Figure 3. Conic decomposition of $\vec{t} = \vec{v} + \lambda \tilde{s}$ at (a) zero margin $\kappa = 0$ and (b) non-zero margin $\kappa > 0$. Given a random Gaussian \vec{t} , \vec{v} is found such that $\|\vec{v} - \vec{t}\|$ is minimized while being on the polar cone \mathcal{S}_κ° . $\lambda \tilde{s}$ is in $\text{cone}(\mathcal{S})$ and \tilde{s} is the projection on the convex hull of \mathcal{S} .

depends only upon the unit direction \hat{v} . For values of \vec{v} such that $g_{\mathcal{S}}(\vec{v})$ is not differentiable, the subgradient is not unique, but $\tilde{s}(\vec{t})$ can be defined uniquely as the particular subgradient that obeys the KKT conditions. We call $\tilde{s}(\vec{t})$ the projection of \vec{t} on the convex hull of the manifold \mathcal{S} , or simply the \mathcal{S} -projection of \vec{t} .

From the KKT conditions, Eq. (15), we can write,

$$F(\vec{t}) = \|\lambda \tilde{s}(\vec{t})\|^2. \quad (19)$$

B. Conic decomposition

The KKT conditions can also be interpreted geometrically in terms of the *conic decomposition* of \vec{t} , which generalizes the notion of the decomposition of vectors onto linear subspaces and their null spaces via Euclidean projection. The *shifted polar cone*, \mathcal{S}_κ° , of the manifold \mathcal{S} is defined as the convex set of points which satisfy

$$\mathcal{S}_\kappa^\circ = \{\vec{z} \in \mathbb{R}^{D+1} \mid \vec{z} \cdot \vec{s} + \kappa \leq 0, \forall \vec{s} \in \mathcal{S}\} \quad (20)$$

and is illustrated for $\kappa = 0$ and $\kappa > 0$ in Fig. 3. For $\kappa = 0$, Eq. (20) is simply the *polar cone* of \mathcal{S} [17]. Equation (15) can then be interpreted as the decomposition of \vec{t} into the sum of two component vectors, \vec{v} is its Euclidean projection onto \mathcal{S}_κ° , and the other component $\lambda \tilde{s}(\vec{t})$ is located in the *convex cone* of \mathcal{S} , $\text{cone}(\mathcal{S}) = \left\{ \sum_{i=1}^{D+1} \alpha_i \vec{s}_i \mid \vec{s}_i \in \mathcal{S}, \alpha_i \geq 0 \right\}$. When $\kappa = 0$, the Moreau decomposition theorem states that the two components are perpendicular: $\vec{v} \cdot (\lambda \tilde{s}(\vec{t})) = 0$ [17, 18]. For non-zero κ , the two components need not be perpendicular but obey $\vec{v} \cdot (\lambda \tilde{s}(\vec{t})) = -\kappa \lambda$.

C. Types of supports

The various \vec{t} vectors contribute in varying amounts to the inverse capacity calculation and represent qualitatively different solutions for \vec{s} and \vec{v} . They can be distinguished by the dimension of the span of the set of the subgradients $\{\partial g_{\mathcal{S}}(\vec{v})\}$, or equivalently, the span of the manifolds' intersection with the margin planes of the solution hyperplane. We call this dimension, the *embedding dimension*, denoted by $0 \leq k \leq D+1$, where the interior regime is characterized by $k = 0$. (See SM, Sec. S2, for additional details and examples).

First, we note that there is a regime of vectors \vec{t} for which the subgradient lies inside the *shifted polar cone*, $\mathcal{S}_{\kappa}^{\circ}$ of the manifold. In this case, the optimal \vec{v} is \vec{t} itself, hence, $\vec{v} = \vec{t}$ and $\lambda = 0$. Hence, this regime does not contribute to the inverse capacity. In terms of the original P manifolds, this regime represents those manifolds that are interior to the margin planes of the solution, hence this regime is denoted the *interior regime*. The condition on \vec{t} belonging to the interior regime is

$$g(\vec{t}) + \kappa < 0 \quad (21)$$

where we drop the explicit subscript \mathcal{S} in the support function $g(\vec{v})$ when the reference manifold is unambiguous. When $\lambda = 0$, (15) does not specify a unique point \vec{s} on the manifold; in this interior regime, we define a unique \mathcal{S} -projection of \vec{t} using Eq. (18):

$$\vec{s}(\vec{t}) = \arg \max_{\vec{s} \in \mathcal{S}} \vec{t} \cdot \vec{s} \quad (22)$$

Non-zero contributions to the inverse capacity only occur outside the interior regime when $g(\vec{t}) + \kappa > 0$, in which case, $\lambda > 0$. In this case, the solution for \vec{v} is *active*, satisfying the equality condition,

$$g(\vec{v}) + \kappa = 0 \quad (23)$$

With regard to the original classification problem, this indicates that the corresponding manifolds overlap with the margin planes of the solution \mathbf{w} . From

$$g(\vec{v}) = \vec{v} \cdot \vec{s}(\vec{t}) = \vec{t} \cdot \vec{s}(\vec{t}) - \lambda \|\vec{s}(\vec{t})\|^2 = -\kappa \quad (24)$$

we obtain, $\lambda = \frac{(\vec{t} \cdot \vec{s}(\vec{t}) + \kappa)}{\|\vec{s}(\vec{t})\|^2}$ so that from Eq. (19),

$$F(\vec{t}) = \frac{(\vec{t} \cdot \vec{s}(\vec{t}) + \kappa)^2}{\|\vec{s}(\vec{t})\|^2} \quad (25)$$

The following combined expression is valid for both the interior and non-interior regimes,

$$\lambda = \frac{[\vec{t} \cdot \vec{s}(\vec{t}) + \kappa]_+}{\|\vec{s}(\vec{t})\|^2} \quad (26)$$

where the function $[x]_+ = \max(x, 0)$. Thus, the inverse capacity, Eq. (19), can be written in the useful form:

$$\alpha_M^{-1}(\kappa) = \left\langle \frac{[\vec{t} \cdot \vec{s}(\vec{t}) + \kappa]_+^2}{\|\vec{s}(\vec{t})\|^2} \right\rangle_{\vec{t}} \quad (27)$$

where the expectation is over $D+1$ dimensional Gaussian \vec{t} with zero mean and unit covariance matrix and $\vec{s}(\vec{t})$ is the \mathcal{S} -projection of \vec{t} . Regimes with $k > 0$ can be further classified as in the following:

Touching ($k = 1$): In this case, \vec{t} lies slightly outside $\mathcal{S}_{\kappa}^{\circ}$ and the corresponding \vec{v} is on the boundary of $\mathcal{S}_{\kappa}^{\circ}$ near \vec{t} . The subgradient $\partial g_{\mathcal{S}}(\vec{v})$ is unique and the projection $\vec{s}(\vec{t})$ is on the boundary of the manifold. This solution corresponds to manifolds that touch the solution margin plane at a single *support vector*.

Fully embedded ($k = D+1$): In this region, \vec{t} lies within the convex cone, $\text{cone}(\mathcal{S})$. The corresponding \vec{v} is at the point of $\mathcal{S}_{\kappa}^{\circ}$ nearest the origin, i.e., $\vec{v} = -\frac{\kappa}{c}\hat{c}$. The set of subgradients $\partial g_{\mathcal{S}}(\vec{v})$ is the entire convex hull, $\text{conv}(\mathcal{S})$, and the \mathcal{S} -projection $\vec{s}(\vec{t})$ is in the interior of $\text{conv}(\mathcal{S})$. This case corresponds to the fraction of manifolds that completely overlap the margin planes, which we denote as *fully embedded* support manifolds. In this case, the contribution to the inverse capacity is given by,

$$F(\vec{t}) = \left\| \vec{t} + \frac{\kappa}{c}\hat{c} \right\|^2 \quad (28)$$

Partially embedded ($1 < k \leq D$): If the convex hull $\text{conv}(\mathcal{S})$ is *strictly* convex, its boundary does not contain faces with dimension larger than unity. Hence, only interior, touching, or fully embedded regions exist; an example of such manifolds are ℓ_2 ellipsoids discussed in Sec. VI.

On the other hand, if $\text{conv}(\mathcal{S})$ is not strictly convex, partially embedded regimes for which $1 < k \leq D$ may exist. An example, described in Sec. VII, is ℓ_1 ellipsoids. It is important to note that even smooth manifolds with finite differentiable curvature everywhere may have convex hulls which contain faces. An example described in Sec. VIII is that of *orientation manifolds*, defined by $\mathbf{x}^{\mu}(\theta)$ which are periodic differentiable functions of a single angle, and which display interesting partially embedded support structures.

D. Mixtures of manifold geometries

We previously assumed that each of the P manifolds had the same affine dimension and geometry, described by the set \mathcal{S} . We extend our theory to heterogeneous manifolds, which are described by a set $\{\mathcal{S}_l\}$ where $l = 1, \dots, L$ denotes the different manifold shapes. In the replica theory, the shape of the manifolds appear only in the free energy

term, G_1 (see Appendix, Eq. (A.13)). For a mixture of shapes, the combined free energy is given by simply averaging each of the individual free energy terms for \mathcal{S}_l . Recall that this free energy term determines the capacity for each shape, giving an individual inverse critical load $\alpha_{\mathcal{S}_l}^{-1}$. The inverse capacity of the heterogeneous mixture is then,

$$\alpha_{\{\mathcal{S}_l\}}^{-1} = \langle \alpha_{\mathcal{S}_l}^{-1} \rangle_l \quad (29)$$

where the average is over the fractional proportions of manifold geometries. This remarkably simple but generic theoretical result enables analyzing diverse manifold classification problems, consisting of mixtures of manifolds with varying dimensions, shapes and sizes.

Eq. (29) assumes each manifold is assigned a binary label independent of its geometrical shape or dimension. But in more complex scenarios, the binary label of a manifold may be correlated with its underlying geometry. For instance, the positively labelled manifolds may consist of one geometry and the negatively labelled manifolds may have a different geometry. How do structural differences between the two classes affect the capacity of the linear classification? A linear classifier can take advantage of these correlations by adding a non-zero bias. Previously, it was assumed that the optimal separating hyperplane passes through the origin; this is reasonable when the two classes are statistically the same. However, when there are statistical differences between the two classes, Eq. (2) should be replaced by $y^\mu(\mathbf{w} \cdot \mathbf{x}^\mu - b) \geq \kappa$ where the bias b is chosen to maximize the capacity. The effect of optimizing the bias is discussed in more detail in Sec. IX and in SM (Sec. S3).

E. Numerical methods

The solution of the mean field equations consists of two stages. First, \tilde{s} is computed for a given \tilde{t} and then the relevant contributions to the inverse capacity are averaged over the Gaussian distribution of \tilde{t} . For simple geometries, the first step may be solved analytically, such as for ℓ_2 ellipsoids. However, for more complicated geometries, both steps need to be performed numerically. The first step involves determining \vec{v} and \tilde{s} for a given \tilde{t} by solving the quadratic optimization problem Eq. (14) over the manifold \mathcal{S} . This optimization problem is a quadratic semi-infinite programming (QSIP) problem, since the manifold \mathcal{S} may contain infinitely many points. We have developed a novel “cutting plane” method to efficiently solve the QSIP problem. The details of the algorithm are given in the SM (Sec. S4). Gaussian expectations are computed by sampling \tilde{t} in $D+1$ dimensions and taking the appropriate averages, similar to the procedure for other mean field methods. The relevant quantities cor-

responding to the capacity are quite concentrated and converge quickly with relatively few samples.

In the experimental sections, we have shown how the mean field theory compares with computer simulations that numerically solve for the maximum margin solution of realizations of P manifolds in \mathbb{R}^N , as described by Eq. (2) for a variety of manifold geometries. Finding this solution is challenging as standard methods to solving SVM problems are limited to a finite number of input points. In our simulations, we approximate the maximum margin solution using the method described in [19] and in SM (Sec. S5).

IV. MANIFOLD GEOMETRY

Our theory describes the capacity and the properties of the maximum margin solution in terms of mapping Gaussian distributed vectors \vec{t} to their \mathcal{S} -projection $\tilde{s}(\vec{t})$ in the convex hull, $\text{conv}(\mathcal{S})$. In this section we use this mapping to explore geometric properties of $\text{conv}(\mathcal{S})$, such as effective size and dimension. Our definition of these geometric quantities, are motivated by the linear classification theory and shed light on the relation between geometry and linear separability. More generally, these quantities can be viewed as defining novel generalized signal-to-noise parameters of the manifolds.

Manifold centers: The theory of manifold classification described in Sec. III is completely general and does not require the notion of a manifold center. However, in order to understand how scaling the manifold sizes by a parameter r affects their capacity, the center points, about which the manifolds are scaled, 4, need to be defined. For many geometries, the center is a point of symmetry, such as for an ellipsoid. For general manifolds, there are various ways to define a center point by averaging points on the manifold using a particular measure. In the present theory, a natural definition of the manifold center is provided by the *Steiner point* for convex bodies [20]:

$$\vec{s}^0 = \langle \nabla g_{\mathcal{S}}(\vec{t}) \rangle_{\vec{t}} \quad (30)$$

where the expectation is over the Gaussian measure of $\vec{t} \in \mathbb{R}^{D+1}$.

The geometric properties of the manifolds important for linear classification are determined by the displacements of the points on the manifold’s convex hull relative to this center point. The set of relative displacement points from the center is defined as, $\vec{s}_\perp = \vec{s} - \vec{s}^0$ where $\vec{s} \in \text{conv}(\mathcal{S})$. The displacement vectors span a D dimensional linear space. In general, a manifold may be shifted along its D dimensional linear span so that the center need not coincide with the orthogonal translation vector \vec{c} (Fig. 2(a)). It is, however, natural to characterize the manifold

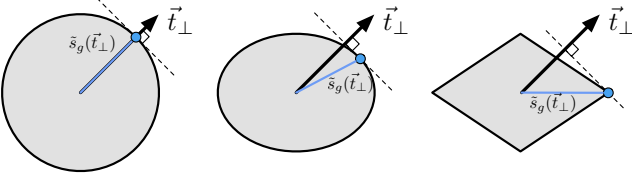


Figure 4. Gaussian geometry. Mapping from \vec{t}_\perp to points $\tilde{s}_g(\vec{t}_\perp)$ for various manifolds: (left) sphere, (middle) ℓ_2 ellipsoid; (right) polytope manifold.

geometry with respect to a configuration where the center and orthogonal translation vector coincide: $\vec{s}^0 = \vec{c}$. We call manifolds with this configuration, *centered manifolds* as illustrated in Fig. 2(b). For simplicity, we will also normalize coordinates so that $\|\vec{s}^0\| = \|\vec{c}\| = 1$. This means that all lengths are defined relative to the distance of the centers from the origin. We can then decompose vectors in \mathbb{R}^{D+1} in terms of their projection on the center vector and their perpendicular components so that $\vec{t} = (\vec{t}_\perp, t_0)$ where $t_0 = \vec{t} \cdot \hat{c}$, and $\vec{s} = (\vec{s}_\perp, 1)$ and $\vec{v} = (\vec{v}_\perp, v_0)$. For brevity, we will use the notation $\vec{s}_\perp \in \mathcal{S}$ to mean $(\vec{s}_\perp, 1) \in \mathcal{S}$ and similarly for other vectors.

For manifolds with centered configurations, the capacity can be written as,

$$\alpha_M^{-1}(\kappa) = \left\langle \frac{[t_0 + \vec{t}_\perp \cdot \vec{s}_\perp(\vec{t}) + \kappa]_+^2}{1 + \|\vec{s}_\perp(\vec{t})\|^2} \right\rangle_{\vec{t}} \quad (31)$$

implying that the geometric characterization of the manifolds should focus on the statistics of $\|\vec{s}_\perp(\vec{t})\|$ and $\vec{t}_\perp \cdot \vec{s}_\perp(\vec{t})$, where $\hat{s}_\perp(\vec{t})$ denotes a unit vector in the direction of $\vec{s}_\perp(\vec{t})$.

A. Gaussian geometry

A simple mapping from \vec{t} to points $\tilde{s}_g \in \text{conv}(\mathcal{S})$ that is suggested by our theory is

$$\tilde{s}_g(\vec{t}_\perp) = \nabla g(\hat{t}_\perp) - \vec{s}^0 \quad (32)$$

where \hat{t}_\perp is a unit vector in the direction of \vec{t}_\perp . Here, each Gaussian vector is mapped onto the gradient of the support function, given by the displacement point in \mathcal{S} that has maximal overlap with \hat{t}_\perp . We will call the statistics defined by this procedure *Gaussian geometry*, motivated by its relationship with the well-known Gaussian mean width of a convex body [21]. We denote Gaussian geometric quantities with the subscript g , and note that the parameters t_0 and κ have no influence on these quantities since the point of maximal overlap with \vec{t} depends only upon \vec{t}_\perp .

Gaussian manifold radius: The Gaussian manifold radius, denoted by R_g , measures the mean square amplitude of \vec{s}_\perp , i.e.,

$$R_g^2 = \left\langle \|\tilde{s}_g(\vec{t}_\perp)\|^2 \right\rangle_{\vec{t}_\perp} \quad (33)$$

Gaussian manifold dimension: The Gaussian manifold dimension, D_g , characterizes the number of orthogonal directions containing the variability of the manifold, and is defined as

$$D_g = \left\langle (\vec{t}_\perp \cdot \hat{s}_g(\vec{t}_\perp))^2 \right\rangle_{\vec{t}_\perp} \leq \left\langle \|\vec{t}_\perp\|^2 \right\rangle = D \quad (34)$$

where $\hat{s}_g(\vec{t}_\perp)$ is the unit vector in the direction of $\tilde{s}_g(\vec{t}_\perp)$. Thus, D_g scales the affine dimension D by the averaged square of the cosine of the angle between the Gaussian vector \vec{t} and its maximal projection point. While R_g^2 measures the total variance of the manifold, D_g measures the angular spread of the manifold.

The geometric intuition behind these definitions is shown in Fig. 4. For each Gaussian vector $\vec{t}_\perp \in \mathbb{R}^D$, the hyperplane normal to \vec{t}_\perp is translated until it just touches the manifold. Aside from a set of measure zero, for each \vec{t}_\perp the touching point is a unique point on the boundary of $\text{conv}(\mathcal{S})$. The radii and dimension measure the second order statistics of the touching points and their projection on \vec{t}_\perp . The Gaussian geometry is related to the well known *Gaussian mean width* of convex bodies, $w(\mathcal{S}) = 2 \langle g_S(\vec{t}_\perp) \rangle_{\vec{t}_\perp}$ [22].

For the case of D -dimensional ℓ_2 balls with radius R , $\tilde{s}_g(\vec{t}_\perp)$ is just the point on the boundary of the ball in the direction of \vec{t}_\perp ; hence, $R_g = R$ and $D_g = D$. However, for general manifolds, D_g can be much smaller than the manifold affine dimension D as will be seen in some examples later.

B. Polar-constrained geometry

In the limit of small manifold sizes, the Gaussian geometry is sufficient for describing the linear classification capacity, as will be shown in Sec. IVD. However, for manifolds with substantial extent, \vec{t} may violate the constraint $g(\vec{t}) \leq -\kappa$ and we need to consider statistics that represent valid solution vectors, and not simply the maximal projection point $\nabla g(\vec{t})$. A natural extension of the Gaussian geometry is provided by the KKT analysis, namely,

$$\tilde{s}_\perp(\vec{t}) = \tilde{s}(\vec{t}) - \vec{s}^0 \quad (35)$$

where $\tilde{s}(\vec{t})$ is the \mathcal{S} -projection of \vec{t} , defined by Eq. (16). Here $\vec{v} = (\vec{v}_\perp, v_0)$ is the closest vector in the polar cone \mathcal{S}_κ° to \vec{t} that satisfies the separability conditions in Eq.

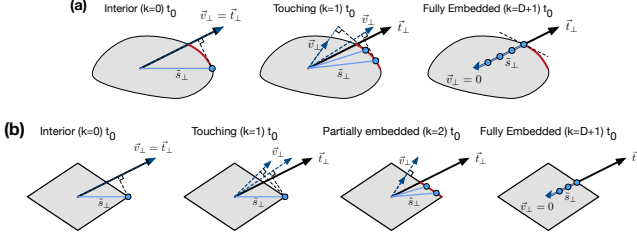


Figure 5. Polar-constrained geometry. Determining \tilde{s}_\perp for different values of t_0 for (a) strictly convex manifold and (b) polytope manifold. In the interior regime ($k = 0$), \tilde{s}_\perp is the same as $\nabla g(\vec{t}_\perp)$ used for the Gaussian geometry. In other regimes, \vec{v} needs to be self-consistently determined. In the fully embedded regime, $\vec{v}_\perp = 0$ and \tilde{s}_\perp lies in the interior of the manifold.

(14), and $\tilde{s} = (\tilde{s}_\perp, 1)$ is the unique subgradient of \vec{v} in Eq. (15). Since $g(\vec{v}) = g(\vec{v}_\perp) + v_0$, we have,

$$g(\vec{v}_\perp) = \max_{\tilde{s}_\perp} \{ \vec{v}_\perp \cdot \tilde{s}_\perp \mid \tilde{s}_\perp \in \mathcal{S} \}, \quad (36)$$

and the constraint, $g(\vec{v}_\perp) \leq -(v_0 + \kappa)$.

Fig. 5 illustrates how the polar-constrained geometry captures the statistics of the subgradient that obeys the margin inequality. We will keep the definition of the center as the Steiner Point in Eq. (30), since it represents the limit point on the manifold when the manifold size shrinks to zero. However, other properties for the polar-constrained geometry will differ from the Gaussian counterparts.

Polar-constrained manifold radius: The manifold radius R_M is given by,

$$R_M^2 = \left\langle \|\tilde{s}_\perp(\vec{t})\|^2 \right\rangle_{\vec{t}} \quad (37)$$

Polar-constrained manifold dimension: The manifold radius D_M is given by

$$D_M = \left\langle (\vec{t}_\perp \cdot \hat{s}_\perp(\vec{t}))^2 \right\rangle_{\vec{t}} \leq D \quad (38)$$

where $\hat{s}_\perp(\vec{t})$ is a unit vector in the direction of $\tilde{s}_\perp(\vec{t})$.

The polar-constrained geometric properties offer a richer description of the manifold properties relevant for classification. Since \vec{v}_\perp and \tilde{s}_\perp depend in general on $t_0 + \kappa$, the above quantities are averaged not only over \vec{t}_\perp but also over t_0 . For the same reason, the quantities also depend upon the imposed margin, since the shifted polar cone \mathcal{S}_κ° depends upon κ .

Under a change in scale, the Gaussian radius R_g scales linearly with the scale factor r and D_g is invariant. In contrast, the polar-constrained R_M need not scale linearly with r , and D_M may vary as well. This is because the classification properties of manifolds are not invariant to a change in scale if the center distances are kept fixed.

Gaussian properties ignore the effect of the relative scale between manifold size and center distances, whereas the polar-constrained geometrical quantities account for this scale change on classification performance. Thus, the polar-constrained quantities can be viewed as describing the general relationship between the signal (center distance) to noise (manifold variability) in classification capacity.

C. Embedding regimes

As discussed previously, the interior region of \vec{t} does not contribute to capacity. In this region, the definition of $\tilde{s}_\perp(\vec{t})$ for the polar-constrained geometry is equivalent to the Gaussian geometry $\tilde{s}_g(\vec{t})$. However, for the non-interior regions, the vector \vec{v} does not correspond to \vec{t} and lies in the relative interior of a face of the shifted polar cone. We have described a partitioning of these regions into corresponding embedded regions with dimension $k \geq 1$. This has a major effect on the geometrical quantities, since the induced measure becomes concentrated on sets of $\tilde{s}_\perp(\vec{t})$ that have zero measure in the Gaussian geometry. In particular, when the manifold becomes fully embedded, $\tilde{s}_\perp(\vec{t})$ is in the *interior of the convex hull* and not confined to its boundary. This effect becomes very prominent in the limit of large manifolds.

To understand the consequences of the geometry defined above, it is useful to follow changes in the nature of the mapping in Eq. (35) as t_0 increases from $-\infty$ to $+\infty$ for a fixed \vec{t}_\perp . These changes correspond to changing the dimension of the embedding. Here we summarize the differences in embedding for centered manifolds that are depicted in Fig. 5(b).

1. Interior ($k = 0$): For sufficiently negative t_0 , we see from Eq. (21) that the interior regime will become valid. We can define the transition to the interior region as,

$$t_0 + \kappa < t_{\text{touch}}(\vec{t}_\perp) \quad (39)$$

with the threshold value

$$t_{\text{touch}} = -g(\vec{t}_\perp) \quad (40)$$

2. Touching ($k = 1$): As t_0 increases to $t_{\text{touch}}(\vec{t}_\perp) - \kappa$, the solution corresponds to the touching region with $k = 1$. This solution is valid as long as $\partial g_S(\vec{v}_\perp) = \nabla g_S(\vec{v}_\perp)$ is unique. In this case, \tilde{s}_\perp lies on the boundary of the manifold.

3. Fully embedded ($k = D+1$): This region occurs for \vec{t} such that the corresponding \vec{v} is orthogonal to all the affine displacement vectors of the manifold, i.e., $\vec{v}_\perp = 0$, $v_0 = -\kappa$, and the subgradient is the entire convex hull, $\text{conv}(\mathcal{S})$. In this case, the specific subgradient satisfying the KKT conditions is given by

$$\tilde{s}_\perp(\vec{t}_\perp, t_0) = \frac{\vec{t}_\perp}{t_0 + \kappa} \quad (41)$$

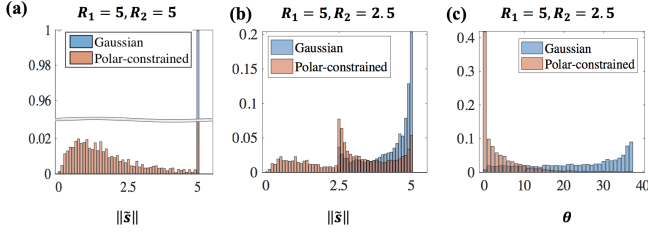


Figure 6. Distribution of $\|\tilde{s}\|$ and $\theta = \angle(\vec{t}, \tilde{s})$ for $D = 2$ ellipsoids. (a) Distribution of \tilde{s} for $D = 2$ ℓ_2 ball with $r = 5$. Gaussian statistics are peaked at $\|\tilde{s}\| = r$ (blue), while the polar-constrained \tilde{s} 's have non-zero probability in $\|\tilde{s}\| < r$ regime (red). (b-c) $D = 2$ ellipsoids, with radii $R_1 = r = 5$ and $R_2 = \frac{1}{2}r$. (b) Distribution of \tilde{s} for (blue) Gaussian \tilde{s} , (red) Polar-constrained \tilde{s} . (c) Distribution of $\theta = \angle(\vec{t}, \tilde{s})$.

For a fixed \vec{t}_\perp , t_0 must be large enough, $t_0 > t_{\text{embed}}$, where

$$t_{\text{embed}}(\vec{t}_\perp) = \arg \min \left\{ t_0 \mid \frac{\vec{t}_\perp}{t_0 + \kappa} \in \text{conv}(\mathcal{S}) \right\} \quad (42)$$

so that $\tilde{s}_\perp(\vec{t}_\perp, t_0) \in \text{conv}(\mathcal{S})$. We note that the quantity $\lambda = t_{\text{embed}}(\vec{t}_\perp) + \kappa$ is equivalent to the Minkowski norm of \vec{t}_\perp under $\text{conv}(\mathcal{S})$. This norm is given by the smallest scalar λ such that $\vec{t}_\perp \in \lambda \text{conv}(\mathcal{S})$ [21].

4. Partially embedded ($1 < k \leq D$): If $\text{conv}(\mathcal{S})$ is not strictly convex, other types of solutions exist, which correspond to *intermediate* ranges of t_0 such that \vec{v}_\perp is perpendicular to a $(k - 1)$ -dimensional *face* of the convex hull, and \tilde{s}_\perp is the unique \mathcal{S} -projected point on that face. For instance, $k = 2$ implies that \tilde{s}_\perp lies on an edge whereas $k = 3$ implies that \tilde{s}_\perp lies on a planar 2-face of the convex hull. Determining the transition values for t_0 that give different embeddings depend upon the specific geometry of the manifold and given \vec{t}_\perp .

We illustrate these geometrical quantities in Fig. 6 with two simple examples: a $D = 2$ ℓ_2 ball and a $D = 2$ ℓ_2 ellipse. In both cases we consider the distribution of $\|\tilde{s}_\perp\|$ and $\theta = \cos^{-1}(\hat{t}_\perp \cdot \hat{s}_\perp)$, the angle between \vec{t}_\perp and \tilde{s}_\perp . For the ball with radius r , the vectors \vec{t}_\perp and \tilde{s}_\perp are parallel so the angle is always zero. For the Gaussian statistics, the distribution of $\|\tilde{s}_\perp\|$ is a delta function at r . On the other hand, for the polar-constrained geometry, \tilde{s}_\perp will lie inside the ball in the fully embedded region. Thus the distribution of $\|\tilde{s}_\perp\|$ consists of a mixture of a delta function at r corresponding to the interior and touching regions and a smoothly varying distribution corresponding to the fully embedded region. Fig. 6 also shows the corresponding densities for a two dimensional ellipsoid with major and minor radius, $R_1 = r$ and $R_2 = \frac{1}{2}r$. For the Gaussian geometry, the distribution of $\|\tilde{s}_\perp\|$ has finite support between R_1 and R_2 , whereas the polar-constrained geometry has support also below R_2 . Since \vec{t}_\perp and \tilde{s}_\perp need not be parallel, the distribution of the angle varies between zero and $\frac{\pi}{4}$, with

the polar-constrained geometry being more concentrated near zero due to contributions from the embedded region.

D. Size and margin effects

We discuss the effect of the manifold size on its geometric properties. Scaling the manifolds as in Eq. (4), corresponds to scaling all \tilde{s}_\perp by a scalar r . Here we focus on the limits of small and large r . In the limit of small size, $\|\tilde{s}_\perp\| \rightarrow 0$ giving $\vec{t} \cdot \tilde{s} \approx t_0$ and $\|\tilde{s}\|^2 \approx 1$. Here, only the interior and touching regimes contribute to the statistics, and $\vec{v}_\perp = \vec{t}_\perp - \lambda \tilde{s}_\perp \approx \vec{t}_\perp$. Therefore, in this limit, the polar-constrained statistics are equivalent to the Gaussian geometry quantities, $R_M \rightarrow R_g$ and $D_M \rightarrow D_g$. Thus, for small scales r , the manifold dimension $D_M = D_g$ which can be substantially smaller than D .

In the large size limit $\|\tilde{s}_\perp\| \rightarrow \infty$. In this limit, $g(\vec{v}_\perp) > \|\tilde{s}_\perp\| \|\vec{v}_\perp\|$ and from the condition that $g(\vec{v}_\perp) \leq -(v_0 + \kappa)$, we have $\|\vec{v}_\perp\| \leq \frac{-(v_0 + \kappa)}{\|\tilde{s}_\perp\|}$. Since v_0 is order one, \vec{v}_\perp must be small with norm $O(\|\tilde{s}_\perp\|^{-1})$. Thus, in the large size limit, the manifolds are almost parallel to the margin planes, either due to being fully embedded (when $\vec{v}_\perp = 0$) or partially embedded when \vec{v}_\perp is close to zero. Since $\lambda \tilde{s}_\perp = \vec{t}_\perp - \vec{v}_\perp \approx \vec{t}_\perp$, it follows that $D_M \rightarrow D$ as $r \rightarrow \infty$. The interior regime is negligible, so the statistics is dominated by the embedded regimes. In fact, the fully embedded transition is given by $t_{\text{embed}} \approx -\kappa$ so that the fractional volume of the fully embedded regime is $H(-\kappa) = \int_{-\kappa}^{\infty} Dt_0$. The remaining summed probability of the touching and partially embedded regimes ($k \geq 1$) is therefore $H(\kappa)$. The radius R_M also increases with r , but the relative ratio $\frac{R_M}{r}$ will decrease with r because for large r , the distribution of \tilde{s}_\perp has support in the interior of the convex hull (due to the contribution of the fully embedded regime).

For manifolds with large sizes, there are two main contributions to the capacity. The *fully embedded* regime contributes a factor in Eq. (28), $\int_{-\kappa}^{\infty} Dt_0 \left[\langle \|\vec{t}_\perp\|^2 \rangle + (t_0 + \kappa)^2 \right] = H(-\kappa)D + \alpha_0^{-1}(\kappa)$. In the touching and partially embedded regimes, $\lambda^2 \|\tilde{s}\|^2 \approx \lambda^2 \|\tilde{s}_\perp\|^2 \approx \|\vec{t}_\perp\|^2$, so that this regime contributes a factor of $\int_{-\kappa}^{\infty} Dt_0 \langle \|\vec{t}_\perp\|^2 \rangle = H(\kappa)D$. Combining these two contributions, we obtain for large sizes, $\alpha_M^{-1} = D + \alpha_0^{-1}(\kappa)$, consistent with Eq. (8).

The polar-constrained geometry also depends on the margin κ , through the dependencies of \vec{v}_\perp and \tilde{s}_\perp on $t_0 + \kappa$. For a fixed \vec{t} , Eq. (42) implies that larger κ increases the probability of being in the embedded regimes, influencing the statistics of \tilde{s}_\perp . Also, increasing κ shrinks the magnitude of \tilde{s}_\perp according to Eq. (41). Hence, when $\kappa \gg 1$, the capacity becomes similar to that of P random points

and the corresponding capacity is given by $\alpha_M \approx \kappa^{-2}$, independent of manifold geometry.

V. HIGH DIMENSIONAL MANIFOLDS

We expect that in many applications the affine dimension of the manifold, D is large. High dimension can be reflected in the data having a large number of non-zero singular value decomposition (SVD) components. However, second-order statistics may not be sufficient to characterize generic manifolds, and we therefore define high-dimensional manifolds as manifolds where the manifold dimension is large, i.e., $D_M \gg 1$. Thus, in general, this regime depends upon both the shape and on the size of the manifold, through their effect on D_M . For high dimensional manifolds, the classification capacity can be described in terms of the statistics of R_M and D_M alone. Our analysis below elucidates the interplay between size and dimension, namely, how small R_M needs to be for high dimensional manifolds to have a substantial classification capacity.

Sufficient statistics for mean-field solution: In the high-dimensional regime, the mean field equations simplify due to self averaging of terms involving sums of components t_i and \tilde{s}_i . The two key quantities, $\vec{t} \cdot \vec{s}(\vec{t})$ and $\|\vec{s}(\vec{t})\|^2$ that appear in the capacity, (27), can be approximated as,

$$\begin{aligned} \vec{t} \cdot \vec{s} &= t_0 + \vec{t}_\perp \cdot \vec{s}_\perp \\ &\approx t_0 + R_M \sqrt{D} \langle \hat{t}_\perp \cdot \hat{s}_\perp \rangle \\ &\approx t_0 + \kappa_M \end{aligned} \quad (43)$$

where we introduce the effective manifold margin $\kappa_M = R_M \sqrt{D_M}$. Combining with $\|\vec{s}(\vec{t})\|^2 \approx 1 + R_M^2$, we can then write,

$$\lambda \approx \frac{[t_0 + \kappa + \kappa_M]_+}{1 + R_M^2} \quad (44)$$

and obtain for the capacity,

$$\begin{aligned} \alpha_M^{-1}(\kappa) &\approx \frac{1}{1 + R_M^2} \left\langle [t_0 + \kappa + \kappa_M]_+^2 \right\rangle_{t_0} \\ &= \frac{1}{1 + R_M^2} \alpha_0^{-1}(\kappa + \kappa_M) \end{aligned} \quad (45)$$

where α_0^{-1} is the inverse capacity of P random points (details in SM, Sec. S6). Note that in the case of ℓ_2 balls with $D \gg 1$ and radius R , we have shown previously that $\alpha_B \approx (1 + R^2) \alpha_0(\kappa + R\sqrt{D})$ [15]. Hence Eq. (45) can be considered as a spherical approximation, where the capacity of a general high dimensional manifold is similar to that of an ℓ_2 ball with $D = D_M$ and $R = R_M$.

Scaling regime: Eq. (45) implies that to obtain a finite capacity in the high-dimensional regime, the effective margin $\kappa_M = R_M \sqrt{D_M}$ needs to be of order unity

which requires the radius to be small, scaling for large $D_M \gg 1$ as $R_M = O(D_M^{-\frac{1}{2}})$. In this *scaling regime*, the calculation of the capacity and geometric properties are particularly simple. As shown in Sec. IV D, when the radius is small, the components of \vec{s}_\perp are small, hence $\vec{v}_\perp \approx \vec{t}_\perp$, and the Gaussian statistics for the geometry suffice: $R_M \approx R_g$ and $D_M \approx D_g$. The capacity is simply,

$$\alpha_M = (1 + R_g^2) \alpha_0(\kappa + \kappa_g) \quad (46)$$

where $\kappa_g = R_g \sqrt{D_g} = \frac{1}{2} w(\mathcal{S})$ is equal to half the Gaussian mean width [21]. As for the support structure, since the manifold size is small, the only significant contributions arise from the interior ($k = 0$) and touching ($k = 1$) cases. Note that in the scaling regime, the factor proportional to $1 + R_g^2$ in Eq. (46) is the next order correction to the overall capacity.

Beyond the scaling regime: When R_g is not small, the manifold geometrical parameters, R_M and D_M , cannot be adequately described by the Gaussian statistics, R_g and D_g . In this case, the manifold margin $\kappa_M = R_M \sqrt{D_M}$ is large, and so Eq. (45) can be reduced to:

$$\alpha_M(\kappa) \approx \frac{1 + R_M^2}{\kappa_M^2} = \frac{1 + R_M^{-2}}{D_M} \quad (47)$$

since the capacity for points $\alpha_0(\kappa) \approx \kappa^{-2}$ for large margins. For strictly convex high dimensional manifolds with $R_M = O(1)$, the touching and embedding transitions for t_0 are very large which means that only the touching regime ($k = 1$) contributes to the capacity. For other manifolds that are not strictly convex, partially embedded solutions with $k \ll D$ can also contribute to the capacity.

Finally, when R_M is large, the manifold dimension approaches the embedding dimension $D_M \rightarrow D$, as discussed in Sec. IV D and Eq. (47) reduces to $\alpha_M \approx \frac{1}{D}$, as expected.

VI. STRICTLY CONVEX MANIFOLDS: ℓ_2 ELLIPSOIDS

In this section, we consider the problem of binary classifications of strictly convex manifolds described by D -dimensional ellipsoids under the ℓ_2 norm. We assume here and in the examples of the following sections that the manifolds are centered, as defined at the beginning of Sec. IV. Therefore, the ellipsoids can be parameterized by the set of points: $M^\mu = \left\{ \mathbf{x}^\mu = \mathbf{x}_0^\mu + \sum_{i=1}^D s_i \mathbf{u}_i^\mu, y^\mu = \pm 1 \right\}$ where

$$\mathcal{S} = \left\{ \vec{s} = (\vec{s}_\perp, 1) \mid \sum_{i=1}^D \left(\frac{s_i}{R_i} \right)^2 \leq 1 \right\}. \quad (48)$$

The components of \mathbf{u}_i^μ and of the ellipsoids' centers \mathbf{x}_0^μ are i.i.d. Gaussian distributed with zero mean and variance $\frac{1}{\sqrt{N}}$ so that they are orthonormal in the large N limit. The radii R_i represent the principal radii of the ellipsoids relative to the center.

A. Support function

With ellipsoids, the support function in Eq. (13) can be computed explicitly. For a vector $\vec{v} = (\vec{v}_\perp, v_0)$, with non zero \vec{v}_\perp , the support function $g(\vec{v}_\perp)$ is maximized by a vector \vec{s}_\perp which occurs on the boundary of the ellipsoid for non-zero \vec{v}_\perp . Maximizing $\vec{v}_\perp \cdot \vec{s}_\perp$ subject to the constraint that \vec{s}_\perp obeys the equality constraints in Eq. (48), yields,

$$g_S(\vec{v}_\perp) = \|\vec{v}_\perp \circ \vec{R}\| \quad (49)$$

where we denote $\vec{z} \circ \vec{R}$ as the vector whose components are $(\vec{z} \circ \vec{R})_i = z_i R_i$. The boundary point that maximizes g_S is

$$\vec{s}_\perp^i = \frac{v_\perp^i R_i^2}{\|\vec{v}_\perp \circ \vec{R}\|} \quad (50)$$

(see SM, Sec. S7 for details). For a given (\vec{t}_\perp, t_0) , the vector (\vec{v}_\perp, v_0) is determined by Eq. (15) and the analytic solution above can be used to derive an explicit expression for \vec{s}_\perp . The different solution regimes can be categorized as follows.

Interior regime: This regime holds for t_0 obeying the inequality Eq. (39) with

$$t_{\text{touch}}(\vec{t}_\perp) = -\|\vec{t}_\perp \circ \vec{R}\| \quad (51)$$

Here $\lambda = 0$ and resulting in zero contribution to the inverse capacity, $F = 0$. The subgradient is given by the following boundary point on the ellipse, $\vec{s}_\perp^i(\vec{t}_\perp) = \frac{t_\perp^i R_i^2}{\|\vec{t}_\perp \circ \vec{R}\|}$,

Touching regime: The ellipsoid touches the margin planes at a single point in the range, $t_{\text{touch}} < t_0 + \kappa < t_{\text{embed}}$ defined in Eqs. (51) and (42), where

$$t_{\text{embed}}(\vec{t}_\perp) = \sqrt{\sum_i \left(\frac{t_\perp^i}{R_i}\right)^2} \quad (52)$$

The subgradient is a point on the boundary of the ellipse corresponding to

$$\vec{s}_{\text{touch}}^i(\vec{t}_\perp, t_0) = \frac{t_i R_i^2}{\lambda(1 + R_i^2) - (t_0 + \kappa)}, \quad (53)$$

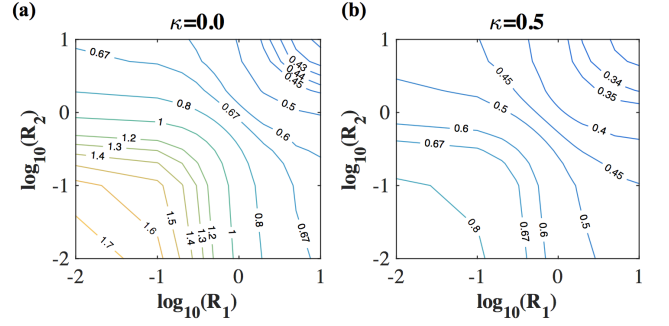


Figure 7. Capacity of $D = 2$ ℓ_2 ellipsoids as a function of the two radii R_1 and R_2 with margin (a) $\kappa = 0$ and (b) $\kappa = 0.5$.

where the parameter λ is determined by the condition

$$1 = \sum_{i=1}^D \frac{t_i^2 R_i^2}{[\lambda(1 + R_i^2) - (t_0 + \kappa)]^2}. \quad (54)$$

In this regime, the contribution to the capacity is given by Eq. (25) with \tilde{s} in Eq. (53). When t_0 approaches the value $t_{\text{embed}} - \kappa$, $\vec{v}_\perp \rightarrow 0$ signalling the transition to the fully embedded regime.

Fully embedded regime: When $t_0 + \kappa > t_{\text{embed}}$, we have $\vec{v}_\perp = 0$, $v_0 = -\kappa$, and $\lambda = t_0 + \kappa$, implying that the center as well as the entire ellipsoid is embedded in the margin plane. In this case, the \mathcal{S} -projection of \vec{t} is given by Eq. (41) which is located in the interior of the ellipsoid and gives a contribution to the capacity in Eq. (28).

Combining the contributions from both the touching and embedded regimes, the capacity for ellipsoids can be written as:

$$\alpha^{-1}(\kappa) = \int D\vec{t}_\perp \int_{\kappa+t_{\text{touch}}(\vec{t}_\perp)}^{\kappa+t_{\text{embed}}(\vec{t}_\perp)} Dt_0 \frac{(\vec{t}_\perp \cdot \vec{s}(\vec{t}) + t_0 + \kappa)^2}{1 + \|\vec{s}(\vec{t})\|^2} + \int D\vec{t}_\perp \int_{\kappa+t_{\text{embed}}(\vec{t}_\perp)}^\infty Dt_0 \left[(t_0 + \kappa)^2 + \|\vec{t}_\perp\|^2 \right] \quad (55)$$

where the limits in the integrals are given by Eq. (51) and (52).

The behavior of the capacity for $2D$ ellipsoids is illustrated in Fig. 7 for margins $\kappa = 0$ and $\kappa = 0.5$. In general, the capacity is higher when $\kappa = 0$ compared with $\kappa = 0.5$. Along the diagonal, the capacity is equivalent to ℓ_2 balls, as $R_1 = R_2$. In particular, for large $R_1 = R_2$ the capacity for $\kappa = 0.0$ approaches 0.4. Along each of the axis one of the ellipse's vanishes, the capacity approaches that of a line, e.g., $\alpha(R_1 \rightarrow 0, R_2, \kappa) = \alpha_1(R_2, \kappa)$ where α_1 is the capacity of one-dimensional line segments with radius R_2 [15]. In particular, when R_2 is large, the capacity approaches $\frac{2}{3}$.

B. High dimensional ellipsoids

It is instructive to apply the general analysis of high dimensional manifolds to ellipsoids with $D \gg 1$. We will distinguish between different size regimes by assuming that all the radii of the ellipsoid are scaled by r , which controls the overall size of the ellipsoid without changing its shape. In the high dimensional regime, due to self-averaging, the boundaries of the touching and embedding transitions can be approximated by,

$$t_{\text{touch}} = -\sqrt{\sum_{i=1}^D R_i^2} \quad (56)$$

$$t_{\text{embed}} = \sqrt{\sum_{i=1}^D R_i^{-2}} \quad (57)$$

both independent of \vec{t}_\perp . Then as long as $R_i\sqrt{D}$ are not large as described below, $t_{\text{embed}} \rightarrow \infty$, and the probability of embedding vanishes. Discounting the embedded regime, the manifold geometry is described by,

$$\tilde{s}_\perp^i = \frac{R_i^2 t_\perp^i}{Z(1 + R_i^2)} \quad (58)$$

(see Eq. (53)) where the normalization factor Z is given through $Z^2 = \sum_{i=1}^D \frac{R_i^2}{(1+R_i^2)^2}$. The capacity for high-dimensional ellipsoids, Eq. (45), is determined from the manifold radius obeying

$$R_M^2 = \sum_{i=1}^D \frac{R_i^4}{(1 + R_i^2)^2} / \sum_{i=1}^D \frac{R_i^2}{(1 + R_i^2)^2} \quad (59)$$

and manifold dimension D_M ,

$$D_M = \left(\sum_{i=1}^D \frac{R_i^2}{(1 + R_i^2)} \right)^2 / \sum_{i=1}^D \frac{R_i^4}{(1 + R_i^2)^2} \quad (60)$$

We can also compute the covariance matrix of \tilde{s}_\perp . This matrix is diagonal in the basis corresponding to the principal directions of the ellipsoid with eigenvalues,

$$\lambda_i = \frac{R_i^2}{Z(1 + R_i^2)} \quad (61)$$

The above geometrical measures can be related to the eigenvalues of the covariance matrix according to $R_M^2 = \sum_{i=1}^D \lambda_i^2$ and $D_M = \left(\sum_{i=1}^D \lambda_i \right)^2 \left(\sum_{i=1}^D \lambda_i^2 \right)^{-1}$. D_M is equivalent to the *participation ratio* of a covariance matrix with eigenvalues λ_i [23, 24]. For a spherical ball where all the eigenvalues are equal, $D_M = D$; however, when one eigenvalue dominates, the dimension is $D_M \approx 1$. Note that R_M and D_M are not invariant to scaling the ellipsoid by a global factor r , reflecting the important

role of the centers which do not scale. We discuss several important limits below.

Scaling regime: In the scaling regime where the radii are small, the radius and dimension are equivalent to the Gaussian geometry:

$$R_g^2 = \frac{\sum_{i=1}^D R_i^4}{\sum_{i=1}^D R_i^2} \quad (62)$$

$$D_g = \frac{\left(\sum_{i=1}^D R_i^2 \right)^2}{\sum_{i=1}^D R_i^4} \quad (63)$$

and the effective margin is given as,

$$\kappa_g = \left(\sum_{i=1}^D R_i^2 \right)^{1/2} \quad (64)$$

In this regime, the dimension is given by the participation ratio of a covariance matrix whose eigenvalues are the set of ellipsoid squared radii R_i^2 . D_g is also invariant to scaling of the radii by r and $R_g \propto r$ as expected. The capacity is given by $\alpha_M \approx (1 + R_g^2)\alpha_0(\kappa + \kappa_g)$, and the ellipsoids are either interior or touching.

Beyond the scaling regime: When $R_i = O(1)$ all the ellipsoids are touching manifolds since $t_{\text{touch}} \rightarrow -\infty$ and $t_{\text{embed}} \rightarrow \infty$. The capacity is small because $\kappa_M \gg 1$, and is given by $\alpha_M \approx (1 + R_M^2)\kappa_M^{-2}$ with R_M and κ_M in Eqs. (59)-(60). When all $R_i \gg 1$, we have,

$$R_M^2 = \frac{D}{\sum_{i=1}^D R_i^{-2}} = \frac{1}{\langle R_i^{-2} \rangle_i} \quad (65)$$

$D_M = D$, and $\alpha^{-1} = D$. The ellipsoids become fully embedded when $R_i \approx \sqrt{D}$ or larger. In this case, the transition value t_{embed} is order one and the probability of embedding becomes significant.

C. Numerical examples

We illustrate the behavior of high D -dimensional ellipsoids with a bimodal distribution of radii. In Fig. 8, the properties of ellipsoids with radii R_i , where $R_i = r$, for $1 \leq i \leq 95$ $R_i = 0.1r$, for $96 \leq i \leq 100$, are shown as a function of the overall scale r . Fig. 8(a) shows that the mean field theory agrees with the spherical approximation with corresponding R_M and D_M . As seen in (b)-(d), the system is in the scaling regime for $r < 0.3$. In this regime, the manifold dimension is constant and equals $D_g \approx 14$, as predicted by the participation ratio, Eq. (63). In this regime, the manifold radius R_g is linear with r , as expected from Eq. (62). The ratio $\frac{R_g}{r} \approx 0.9$ is close to unity, indicating that in the scaling regime, the

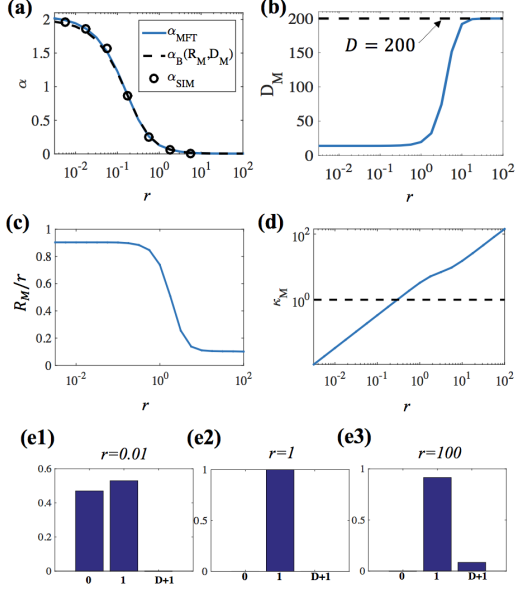


Figure 8. Bimodal ℓ_2 ellipsoids. (a) Classification capacity as a function of scaling factor r : (blue lines) full mean field theory capacity, (black dashed) approximation of the capacity as that of a ball with R_M and D_M , (circles) simulation capacity. (b) Manifold dimension D_M as a function of r . (c) Manifold radius R_M relative to r , as a function of r . (d) $\kappa_M = R_M \sqrt{D_M}$ as a function of r . (e) Fraction of embedding dimensions k for different values of r : (e1) $r = 0.01$, (e2) $r = 1$, (e3) $r = 100$.

system is dominated by the largest radii. For $r > 0.3$ the ellipsoid margin is larger than 1 and the system's properties become increasingly affected by the full dimension of the ellipsoid, as seen by the marked increase in dimension as well as a decrease in $\frac{R_M}{r}$. For larger r , D_M approaches D and $\alpha_M^{-1} = D$. Fig. 8(e1)-(e3) shows the distributions of the embedding dimension $0 \leq k \leq D+1$. In the scaling regime, the interior and touching regimes each have probability close to $\frac{1}{2}$ and the embedding regime is negligible. As r increases beyond the scaling regime, the interior probability decreases and the solution is almost exclusively in the touching regime. For very high values of r , the embedded support solution gains a substantial probability. Note that the capacity decreases to approximately $\frac{1}{D}$ for a value of r below where a substantial fraction of solutions are embedded. In this case, the touching ellipsoids all have small very angle with the margin plane.

We also computed the capacity on ellipsoids containing a more realistic distribution of radii. We have taken as examples, a class of images from ImageNet [25], and analyzed the SVD spectrum of the representations of these images in the last readout layer of a deep convolutional network, GoogLeNet [26]. The computed radii are shown in Fig. 9(a) and are scaled by a overall factor r in our analysis. Because of the fall-off in the distribution of

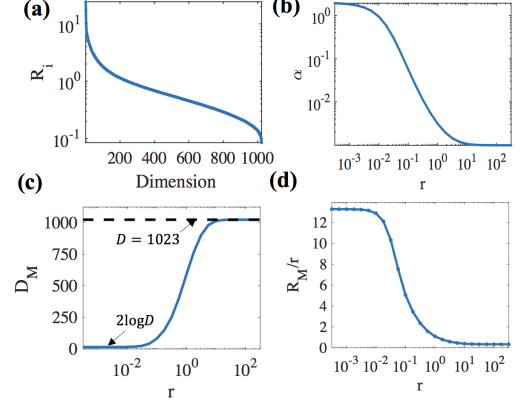


Figure 9. Ellipsoids with radii computed from image data. (a) SVD spectrum, R_i , taken from the readout layer of GoogLeNet from a class of ImageNet images with $N = 1024$ and $D = 1023$. The radii are scaled by a factor r : $R'_i = r R_i$ for (b) Classification capacity as a function of r . (c) Manifold dimension as a function of r . (d) Manifold radius as a function of r .

radii, the Gaussian dimension for the ellipsoid is only about $D_g \approx 15$, much smaller than the affine dimension $D = 1023$. As r increases above $r \gtrsim 0.03$, κ_M becomes larger than 1 and the solution leaves the scaling regime, resulting in a rapid increase in D_M and a rapid falloff in capacity as shown in Fig. 9(b-c). Finally, for very large $r \approx 10$, we have $\alpha_M^{-1} \approx D_M \approx D$ approaching the lower bound for capacity as expected.

VII. CONVEX POLYTOPES: ℓ_1 BALLS

The family of ℓ_2 ellipsoids is a prototypical example of a manifold whose convex hull is *strictly* convex and consists only of vertices and no other faces. This implies that the ℓ_2 ellipsoids can only display three types of support: interior, touching at a single point, or fully embedded. On the other hand, there are other types of manifolds whose convex hulls are not strictly convex. In this section, we consider manifolds that are convex polytopes formed by the convex hulls of finite numbers of points in \mathbb{R}^N . A particularly simple example is provided by a D -dimensional ℓ_1 ellipsoid, parameterized by radii $\{R_i\}$ and specified by the convex set:

$$S = \left\{ \vec{s} = (\vec{s}_\perp, 1) \mid \sum_{i=1}^D \frac{|s_\perp^i|}{R_i} \leq 1 \right\}. \quad (66)$$

Each manifold $M^\mu \in \mathbb{R}^N$ is centered at \mathbf{x}_0^μ and consists of a convex polytope with a finite number ($2D$) of vertices: $\{\mathbf{x}_0^\mu \pm R_k \mathbf{u}_k^\mu, k = 1, \dots, D\}$. The vectors \mathbf{u}_i^μ specify the principal axes of the ℓ_1 ellipsoids.

For simplicity, we consider the case of ℓ_1 balls when all the radii are equal: $R_i = r$. We will concentrate on when

the ℓ_1 balls are high-dimensional; the case for ℓ_1 balls with $D = 2$ was briefly described in [15].

High-dimensional ℓ_1 balls, scaling regime: In the scaling regime, we have $\vec{v} \approx \vec{t}$. In this case, we can write the solution for the subgradient as:

$$\tilde{s}_\perp^i(\vec{t}_\perp) = \begin{cases} r \operatorname{sign}(t_\perp^i), & |t_\perp^i| > |t_\perp^j| \forall j \neq i \\ 0 & \text{otherwise} \end{cases} \quad (67)$$

In other words, $\tilde{s}_\perp(\vec{t}_\perp)$ is a vertex of the polytope corresponding to the component of \vec{t}_\perp with the largest magnitude. The components of \vec{t}_\perp are i.i.d. Gaussian random variables, and for large D , its maximum component is concentrated around $\sqrt{2 \log D}$; hence, $D_g = 2 \log D$ which is much smaller than D . This result is consistent with the fact that the Gaussian mean width of a D -dimensional ℓ_1 ball scales with $\sqrt{\log D}$ and not with D [21]. Since all the points have norm R , we have $R_g = r$, and the effective margin is then given by $\kappa_M = r\sqrt{2 \log D}$, which is order one in the scaling regime. In this regime, the capacity is given by simple relation $\alpha_M = (1 + r^2) \alpha_0 (\kappa + \kappa_M)$.

High-dimensional ℓ_1 balls, $r = O(1)$: When the radius r is small as in the scaling regime, the only contributing solution is the *touching* solution ($k = 1$). When r increases, solutions with all values of k , $1 \leq k \leq D + 1$ occur, and the support can be any of the faces of the convex polytope with dimension k . As r increases, the probability distribution $p(k)$ over k of the solution shifts to larger values. Finally, for large r , only two regimes dominate: fully embedded ($k = D + 1$) with probability $H(-\kappa)$ and partially embedded with $k = D$ with probability $H(\kappa)$.

For convex polytopes at zero margin, $\kappa = 0$, the capacity can be related to the probability distribution $p(k)$: $\alpha^{-1} = \sum_{k=1}^{D+1} p(k)k$ [27], so the shift to higher dimensional support is related to a decrease in capacity. Unfortunately, this simple relationship does not hold for smooth manifolds or for convex polytopes with non-zero margin $\kappa \neq 0$.

Numerical examples: We illustrate the behavior of ℓ_1 balls with radius r and affine dimension $D = 100$. In Fig. 10, (a) shows the linear classification capacity as a function of r . When $r \rightarrow 0$, the manifold approaches the point capacity, $\alpha_M \approx 2$, and when $r \rightarrow \infty$, $\alpha_M \approx \frac{1}{D} = 0.01$. In (b), for the scaling regime of $r < 0.1 = \frac{1}{\sqrt{D}}$, $R_M \approx r$, but when $r \gg 1$, R_M is much smaller than r . In (c), we see $D_M \approx 2 \log D$ in the scaling regime, while $D_M \rightarrow D$ as $r \rightarrow \infty$. In terms of the support structures, when $r = 0.001$ in the scaling regime (d1), most manifolds are either interior or touching. For intermediate sizes (d2), the embedding dimension is peaked at an intermediate value,

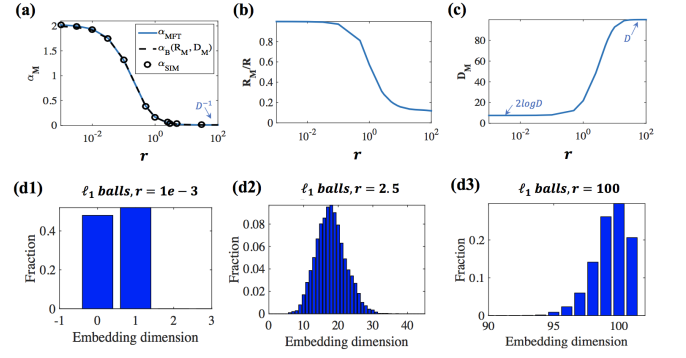


Figure 10. ℓ_1 balls. (a) Linear classification capacity of ℓ_1 balls as function of radius r with $D = 100$ and $N = 200$: (blue) MFT solution, (black dashed) spherical approximation, (circle) full numerical simulations. (b) Manifold radius R_M relative to the actual radius r . (c) Manifold dimension D_M as a function of r . Distribution of embedding dimensions: (d1) $r = 0.001$, (d2) $r = 2.5$, (d3) $r = 100$.

and finally for very large manifolds (d3), most polytope manifolds are nearly fully embedded.

VIII. ORIENTATION MANIFOLDS

An important example of an object manifold is the set of neuronal responses to an object subject to a one-dimensional rotation. Here we consider the simplest case of the rotation of an image, parameterized by an orientation angle θ . We model the neuronal responses as smooth periodic functions of θ , which can be parameterized in terms of Fourier modes in $\vec{s} = (\vec{s}_\perp, 1) \in \mathcal{S}$ with

$$\begin{aligned} s_\perp^{2n}(\theta) &= \frac{R_n}{\sqrt{2}} \cos(n\theta) \\ s_\perp^{2n-1}(\theta) &= \frac{R_n}{\sqrt{2}} \sin(n\theta) \end{aligned} \quad (68)$$

where R_n is the magnitude of the n -th Fourier component for $1 \leq n \leq \frac{D}{2}$. The neural responses in Eq. (1) are determined by projecting onto the basis:

$$\begin{aligned} \mathbf{u}_{2n}^\mu &= \sqrt{2} \cos(n\theta_n^\mu) \\ \mathbf{u}_{2n-1}^\mu &= \sqrt{2} \sin(n\theta_n^\mu) \end{aligned} \quad (69)$$

with centers at \mathbf{u}_{2D+1}^μ . The parameters θ_n^μ are the preferred orientation angles for the corresponding neurons and are assumed to be evenly distributed between $-\pi \leq \theta_i^\mu \leq \pi$.

The statistical assumptions of our analysis assume that the different manifolds are randomly positioned and oriented with respect to the others. For this orientation manifold model, this implies that the mean responses \mathbf{u}_{2D+1}^μ are independent random Gaussian vectors and

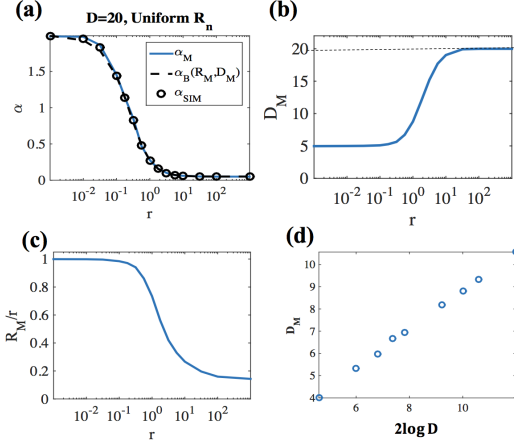


Figure 11. Linear classification of D -dimensional orientation manifolds, with uniform $R_n = \sqrt{\frac{2}{D}}r$. (a) Classification capacity for $D = 20$ as function of r with $m = 200$ test samples (details of numerical simulations in SM, Sec. S9): (blue) mean field theory, (black dashed) spherical approximation, (black circles) numerical simulations. (b) Manifold dimension D_M . (c) Manifold radius ratio $\frac{R_M}{r}$. (d) Manifold dimension compared with $2 \log D$ for small $r = \frac{1}{2\sqrt{D}}$ in the scaling regime.

also that the preferred orientation θ_n^μ angles are uncorrelated. The neuronal tuning curves are unimodal and symmetric functions since the Fourier components have zero phase relative to each other. We could have also chosen random phases for the Fourier components which would have resulted in asymmetric tuning curves. With this definition for the orientation manifold, all the vectors $\vec{s}_\perp \in \mathcal{S}$ obey the normalization $\|\vec{s}_\perp\| = r$ where $r^2 = \sum_{n=1}^{\frac{D}{2}} R_n^2$.

The orientation manifolds are thus smooth closed curves parameterized by a single angle θ that lie on the surface of a D -dimensional sphere with radius r . For the simplest case of $D = 2$, the orientation manifold is equivalent to a circle in two dimensions. However, for larger D , the manifold is not convex and its convex hull is composed of faces with varying dimensions. In Fig. 11, we investigate the geometrical properties of these manifolds relevant for classification as a function of the overall scale factor r , where for simplicity we have chosen $R_n = r$ for all n . The most striking feature is the small dimension in the scaling regime, scaling roughly as $D_M \approx 2 \log D$. This dependence is similar to that of the ℓ_1 ball polytope in the previous section. Thus, we see as r increases, D_M increases dramatically from $2 \log D$ to D .

The similarity of the orientation manifold convex hull to a convex polytope is also seen in the embedding dimension k of the manifolds. Support faces of dimension $k \neq 0, 1, D + 1$ are seen, implying the presence of partially embedded solutions. Interestingly, $\frac{D}{2} < k \leq D$ are excluded, indicating that the maximal face dimension of

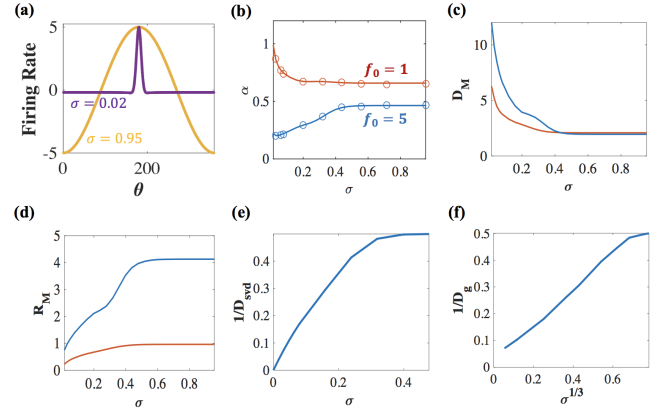


Figure 12. Effect of tuning width on the geometric properties of orientation manifolds. (a) Tuning curve of a neuron with a preferred angle at 180° for various σ . (b) Classification capacity of $D = 300$ orientation manifolds, as a function of a tuning width, σ , for high modulation, $f_0 = 5$ (blue) and small modulation $f_0 = 1$ (red) with (lines) mean field theory and (circles) numerical simulation. (c) Manifold dimension D_M as a function of the tuning width σ . (d) Manifold radius R_M as a function of the tuning width σ . (e) Inverse SVD dimension, $\frac{1}{D_{\text{SVD}}}$. (f) Gaussian dimension $\frac{1}{D_g}$ versus $\sigma^{1/3}$ width showing a power law relationship.

the convex hull is $\frac{D}{2}$. Each face is the convex hull of a set of $k \leq \frac{D}{2}$ points where each point is drawn from a pair of Fourier harmonics. The orientation manifolds are closely related to the *trigonometric moment curve*, whose convex hull geometrical properties have been extensively studied [28, 29].

As expected, the classification capacity of the orientation manifolds drops as the size r , relative to the mean activity increases. An interesting question is the effect of the *tuning width* on the classification capacity. To explore this question, we have modeled a family of tuning curves where the Fourier components, R_n , have a Gaussian fall-off with n ,

$$R_n = A \exp \left[-\frac{1}{2} (2\pi(n-1)\sigma)^2 \right], \quad n \geq 1 \quad (70)$$

where the normalization factor A is such that $\sum_n R_n = f_0$. These tuning curves are characterized by two parameters: σ which controls the width of the tuning, and f_0 which controls the modulation amplitude; example tuning curves are shown in Fig. 12(a). Note that, in the large N limit, n is unbounded and σ determines the number of nonzero components, see below.

In Fig. 12(b), we study the effect of the width σ on the capacity. At high modulation, we find that the classification capacity monotonically *increases* with tuning width. This is consistent with the fact that the Fisher information of the orientation angle *decreases* with the tuning width [30]. Interestingly, for moderate or weak tuning

modulation, e.g., $f_0 = 1$, the capacity decreases with increasing tuning width. This demonstrates the complex balance between size and dimension in determining the capacity (further details in SM, Sec. S8). We also examine the dependence of R_M and D_M with the tuning width in Fig. 12(c)-(d). D_M decreases with tuning width since for large widths, there are only a few dominant Fourier components. On the other hand, R_M increases with the tuning width. This is because more power is concentrated on the low-frequency Fourier components when the overall size given by the sum of R_n is held fixed. For narrower tuning, embedded regimes also contribute to decreasing R_M as explained in Sec. IV.

Finally, we examine in more detail the scaling of manifold dimension on the tuning curve width as $\sigma \rightarrow 0$. A general argument based on SVD decompositions suggests that the manifold dimension scales inversely with the tuning width (for $\sigma \ll 1$) [31]. Consistent with this argument, the participation ratio for this system (see Sec. VIB and SM, Sec. S9) is inversely related to σ for small σ , as seen in Fig. 12(e). Surprisingly, the manifold dimension does not scale with $\frac{1}{\sigma}$. For instance, the Gaussian dimension, D_g , shown in Fig. 12(f), appears to be inversely related to $\sigma^{\frac{1}{3}}$, and not with σ , reflecting the complexity of the underlying convex hull.

IX. MANIFOLDS WITH SPARSE LABELS

So far, we have assumed that the number of manifolds with positive labels is approximately equal to the number of manifolds with negative labels. In this section, we consider the case where the two classes are unbalanced such that the number of positively-labeled manifolds is far less than the negatively-labeled manifolds (the opposite scenario is equivalent). We define the sparsity parameter f as the fraction of positively-labeled manifolds so that $f = 0.5$ corresponds to having balanced labels. From the theory of the classification of a finite set of random points, it is known that having sparse labels with $f \ll 0.5$ can drastically increase the capacity [12]. In this section, we investigate how sparsity of manifold labels improves the manifold classification capacity.

If the separating hyperplane is constrained to go through origin and the distribution of inputs is symmetric around the origin, the labeling y^μ is immaterial to the capacity. Thus, the effect of sparse labels is closely tied to having a non-zero bias. We thus consider inequality constraints of the form $y^\mu(\mathbf{w} \cdot \mathbf{x}^\mu - b) \geq \kappa$, and define the bias-dependent capacity of general manifolds with label sparsity f , margin κ and bias b , as $\alpha_M(\kappa, f, b)$. Next, we observe that the bias acts as a positive contribution to the margin for the positively-labeled population and as a negative contribution to the negatively-labeled population. Thus,

$$\alpha_M^{-1}(\kappa, f, b) \equiv f\alpha_M^{-1}(\kappa + b) + (1 - f)\alpha_M^{-1}(\kappa - b) \quad (71)$$

where $\alpha_M(x)$ is the classification capacity *with zero bias* (and hence equivalent to the capacity with $f = 0.5$) for the same manifolds. Note that Eq. (71) is similar to Eq. (29) for mixtures of manifolds. The actual capacity with sparse labels is given by optimizing the above expression with respect to b , i.e.,

$$\alpha_M(\kappa, f) = \max_b \alpha_M(\kappa, f, b) \quad (72)$$

In the following, we consider for simplicity the effect of sparsity for zero margin, $\kappa = 0$. Small-sized manifolds are expected to have capacity that increases upon decreasing f as $\alpha_M(0, f) \propto \frac{1}{f|\log f|}$, similar to P uncorrelated points. On the other hand, when the manifolds are large, the solution has to be orthogonal to the manifold directions so that $\alpha_M(0, f) \approx \frac{1}{D}$. Thus, the geometry of the manifolds play an important role in controlling the effect of sparse labels on capacity.

A. Sparsely labeled ℓ_2 balls

We first investigate the effect of sparse labels for ℓ_2 balls with dimension D , radius r , and $f \ll 1$. For these manifolds, the full mean field equation is given in Appendix B. These equations reveal the following regimes:

Small r regime: For $r < 1$, the ℓ_2 ball capacity, $\alpha_B(f, r, D)$, is equivalent to the capacity for sparsely labeled random points with an effective margin given by $r\sqrt{D}$,

$$\alpha_B(f, R, D) \approx \alpha_0(f, \kappa = r\sqrt{D}) \quad (73)$$

where the capacity of sparsely labeled points is $\alpha_0(\kappa, f) = \max_b \alpha_0(\kappa, f, b)$ from the Gardner theory.

Large r regime: For $r \gtrsim 2$, the dependence of the capacity on f and r is only through the scaled sparsity parameter

$$\bar{f} = f(1 + r^2) \quad (74)$$

The equation for the capacity as a function of \bar{f} and D is given by,

$$\alpha_B^{-1} = \bar{f}\bar{b}^2 + \int_{\bar{b}}^{\infty} dt \chi_D(t)(t - \bar{b})^2 \quad (75)$$

where $\chi_D(t) \propto t^{D-1} \exp(-\frac{t^2}{2})$ is the Chi distribution. The scaled bias, $\bar{b} = \frac{b}{\sqrt{1+r^2}}$, is found by optimizing Eq. (75), yielding

$$\bar{f}\bar{b} = \int_{\bar{b}}^{\infty} dt \chi_D(t)(t - \bar{b}) \quad (76)$$

For $\bar{f} \ll 1$, the capacity grows roughly as

$$\alpha_B \propto (\bar{f} |\log \bar{f}|)^{-1} \quad (77)$$

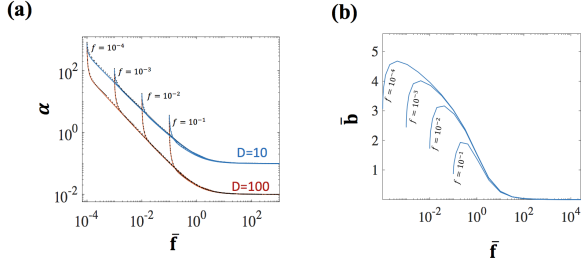


Figure 13. Classification of ℓ_2 Balls with Sparse Labels. (a) Capacity of ℓ_2 balls as a function of $\bar{f} = f(1+r^2)$, for $D = 100$ (red) and $D = 10$ (blue): (solid lines) mean field theory, (dotted lines) is an approximation interpolating between Eqs. (73) and (75) (details in SM, Sec. S9). (b) Effective optimal bias $\bar{b} = b/\sqrt{1+r^2}$ as a function of \bar{f} for ℓ_2 balls with $D = 10$.

with a proportionality constant depending on D . For large \bar{f} , $\alpha_B \approx \frac{1}{D}$, as expected.

The reason for the scaling of f with r^2 is as follows. When the labels are sparse, the dominant contribution to the inverse capacity comes from the minority class, and so the capacity is $\alpha_B^{-1} \approx fb^2$ for large b . On the other hand, the optimal value of b depends on the balance between the contributions from both classes and scales linearly with r , as it needs to overcome the local fields from the spheres. Thus, $\alpha_B^{-1} \propto fr^2$; we have introduced the factor $1+r^2$ instead of r^2 in our scaled variables \bar{f} and \bar{b} for a smoother crossover behavior from small to large r .

Fig. 13 illustrate these regimes for $D = 100$ and 10 ℓ_2 balls, respectively. The capacity is calculated for a sparsity range $10^{-4} \leq f \leq 10^{-1}$ and radius $10^{-2} \leq r \leq 10^3$. The capacity is plotted as a function of scaled sparsity parameter $\bar{f} = f(1+r^2)$. As predicted by Eq. (73), for small values of r , the capacity and scaled optimal bias depend upon both f and r , seen as “vertical branches” in Fig. 13(a)-(b). When $r \gtrsim 2$, we see that the capacity follows a universal curve described by Eq. (74) that depends only upon the scaled parameter \bar{f} . For values of \bar{f} smaller than 1, even for large r , the capacity is substantially enhanced due to sparsity. For large values of \bar{f} , the capacity eventually drops to $\frac{1}{D}$ as expected. Fig. 13 also shows the remarkable agreement between the full mean field theory (solid lines) and the approximation in Eqs. (73) and (75) in both small r and large r regimes (dotted lines).

B. Sparsely labeled general manifolds

A remarkable result for sparsely labeled manifolds with general geometries is that their capacity is well approximated by a *sparse spherical approximation*. In this approximation, the capacity is given by Eqs. (73) and (75) for ℓ_2 balls with dimension $D = D_g$ and radius $r = R_g$, where R_g and D_g are the Gaussian radius and dimension

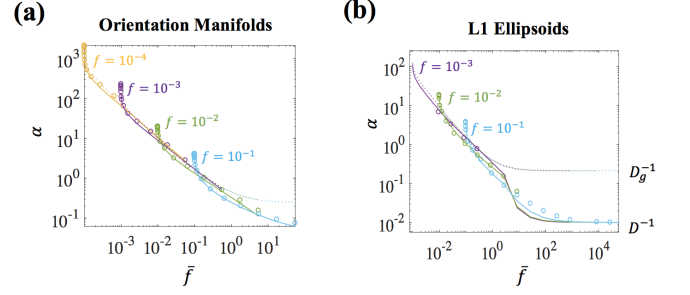


Figure 14. Classification of general manifolds with sparse labels. (a) The capacity of orientation manifolds, Eqs. (68)-(70), with $\sigma = 0.1$, as a function of $f(1+R_g^2)$. Different colors refer to different sparsities f , with varying r by changing the modulation amplitude f_0 from 10^{-3} to 10^3 : (circles) numerical simulations, (lines) mean field theory, (dotted lines) sparse spherical approximation, Eq. (78). (b) Capacity of ℓ_1 ellipsoids with $D = 100$, where the first 10 components are equal to r , and the remaining 90 components are $\frac{1}{2}r$, as a function of $f(1+R_g^2)$. r is varied from 10^{-3} to 10^3 : (circles) numerical simulations, (lines) mean field theory, (dotted lines) spherical approximation.

of the manifold defined in Sec. IV. Interestingly, even though R_g is not necessarily small, we find that the relevant sufficient statistics with sparse labels are given by the Gaussian geometry rather than the polar-constrained values D_M and R_M . The reason is that for small f , the bias is large. In that case, the positively labeled manifolds have large positive margin b and are fully embedded giving a contribution to the inverse capacity of b^2 regardless of their detailed geometry. On the other hand, the negatively labeled manifolds have large negative margin, and exist only in the interior or touching regimes. Hence, their geometry is well approximated by the Gaussian quantities D_g and R_g .

The equivalence between general manifolds and balls with R_g and D_g parameters holds as long as the scaled optimal bias $\bar{b} = b/\sqrt{1+R_g^2} \gg 1$, which occurs when the scaled sparsity is less than 1. Thus, we conclude that for all geometries where $\bar{f} = f(1+R_g^2) \lesssim 1$, the capacity is well approximated by the sparse spherical approximation,

$$\alpha_M(f) \approx \alpha_B(f, R_g, D_g), \quad \bar{f} \lesssim 1 \quad (78)$$

When \bar{f} increases above 1, \bar{b} is small and the capacity is affected by the detailed geometry of the manifold. In particular, as $\bar{f} \gg 1$, the capacity of the manifold approaches $\alpha_M(f) \rightarrow \frac{1}{D}$, not $\frac{1}{D_g}$.

To demonstrate the theory in general manifolds, we have evaluated the capacity of two classes of manifolds: orientation manifolds and ℓ_1 ellipsoids as shown in Fig. 14. For the first examples, we have used the orientation manifold model (Sec. VIII). Fig. 14(a) shows

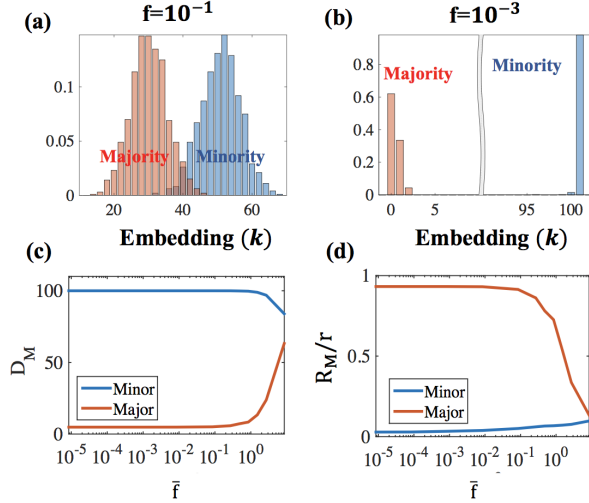


Figure 15. Manifold configurations and geometries for classification of ℓ_1 ellipsoids with sparse labels, analyzed separately in terms of the majority and minority classes. The radii for ℓ_1 ellipsoids are $R_i = r$ for $1 \leq i \leq 10$ and $R_i = \frac{1}{2}r$ for $11 \leq i \leq 100$ with $r = 10$. (a) Histogram of embedding dimensions for moderate sparsity $f = 0.1$: (blue) minority and (red) majority manifolds. (b) Histogram of embedding dimensions for high sparsity $f = 10^{-3}$: (blue) minority and (red) majority manifolds. (c) Manifold dimension as a function of $\bar{f} = f(1 + R_g^2)$ as f is varied: (blue) minority and (red) majority manifolds. (d) Manifold radius relative to the scaling factor r as a function of \bar{f} : (blue) minority and (red) majority manifolds.

that the capacity evaluated by the full mean field theory (solid lines) as well as the numerical simulations (markers) agree well with the sparse spherical approximation (dotted) for $\bar{f} < 1$. Note the similarity with the capacity of the balls (Fig. 13) in both the small and large R_g regimes. The spherical approximation breaks down for $\bar{f} > 1$, rapidly decreasing below the saturation of the approximation, $\frac{1}{D_g}$, for large \bar{f} .

For the example of $D = 100$ ℓ_1 ellipsoids, we used two different values of radii: $D_1 = 10$ components with $R_1 = r$ and $D - D_1$ components with $R_2 = \frac{1}{2}r$. This choice is interesting because in this case, D_g is roughly $2 \log D_1$, much smaller than D . Moreover, R_g is close to r , rather than the average value of R_i which is close to $\frac{1}{2}r$. Fig. 14(b) shows the capacity as a function of \bar{f} (by varying f, r). For the entire range of \bar{f} below 1, the spherical approximation agrees reasonably well with the full mean field as well as simulations. As expected, when $\bar{f} > 1$, the true capacity rapidly decreases and saturates at $\frac{1}{D}$, rather than to the $\frac{1}{D_g}$ limit of the spherical approximation.

As discussed above, in the (high and moderate) sparse regimes, a large bias alters the geometry of the two classes in different ways. To illustrate this important aspect, we show in Fig. 15, the effect of sparsity and bias on the geometry of the ℓ_1 ellipsoids studied in Fig. 14(b). Here

we show the evolution of R_M and D_M for the majority and minority classes as \bar{f} increases. Note that the manifolds have the same shape; nevertheless, their *polar-constrained geometry* depends on both class membership and sparsity levels because these measures depend on the margin. When \bar{f} is small, the minority class has $D_M = D$ as seen in Fig. 15(c), i.e., the minority class manifolds are close to be fully embedded due to the large positive margin. This can also be seen in Fig. 15(a)-(b). On the other hand, the majority class has $D_M \approx D_g = 2 \log D_1 \ll D$, and these manifolds are mostly in the interior regime. As f increases, the geometrical statistics for the two classes become more similar. This is seen in Fig. 15(c)-(d) where D_M and R_M for both majority and minority classes converge to the zero margin value for large $\bar{f} = f(1 + R_g^2)$.

X. SUMMARY AND DISCUSSION

Summary: We have developed statistical mechanical theory for linear classification of points organized in perceptual manifolds, where all points in a manifold share the same label. The notion of perceptual manifolds is critical in a variety of contexts in computational neuroscience modeling and in signal processing. Our theory is not restricted to manifolds with smooth or regular geometries; it applies to any compact subset of a D -dimensional affine subspace. Thus, the theory is applicable to manifolds arising from any variation in neuronal responses with a continuously varying physical variable, or from any sampled set arising from experimental measurements on a limited number of stimuli.

The theory describes the capacity of a linear classifier to separate a dichotomy of general manifolds (with a given margin) by a universal set of mean field equations. These equations may be solved analytically for simple geometries, but for more complex geometries, we have developed iterative algorithms to solve the self-consistent equations. The algorithms are efficient and converge very quickly since they involve only solving for $O(D)$ variables for a single manifold, rather than invoking simulations of full systems of P manifolds embedded in \mathbb{R}^N .

The main goal of our work has been to characterize the dependence of the separation capacity and nature of the maximum-margin separating hyperplane on key features of the geometry of the convex hull of the manifold. In the limit of small manifolds or manifolds with sparse labels, we have shown how the capacity can be statistically described by a Gaussian size R_g and dimension D_g . These geometric measures are induced by choosing points on the boundary of the manifold that have maximum projection on Gaussian random vectors $\vec{\ell}$. The Gaussian geometry is related to well-known size measures in the theory of convex bodies, and differs from standard second-order

statistics based upon SVD analysis with a uniform distribution. In particular, we show how the Gaussian dimension D_g can be much smaller than either the affine dimension D or the dimension computed from SVD.

When the manifolds are large and not sparsely labeled, linear separability is not well described by the Gaussian geometry. Instead, we have introduced new geometrical quantities: the *polar-constrained* manifold radius R_M and dimension D_M that take the geometry of the manifold cone and polar cone into account. Unlike the Gaussian statistics, the polar-constrained statistics depend upon the relative scale r between the manifolds and the size of their centers. In particular, as r increases from zero to infinity, D_M increases from D_g to the full affine dimension D , the latter reflects the fact that for infinitely large manifolds, the solution needs to be orthogonal to all D directions spanned by the manifold relative to its center. Interestingly, we show that the capacity of high dimensional manifolds is well approximated by that of ℓ_2 balls with dimension D_M and radius R_M ,

We also explained how the various manifolds are positioned relative to the separating margin planes at the max-margin solution. There are interior manifolds that do not contribute to the overall capacity, manifolds that touch a margin plane at a single point, and fully embedded manifolds that are wholly contained within a margin plane. For manifold convex hulls that are not strictly convex, there are also partially embedded support manifolds that display the richness of the convex hull geometry with the existence of embedded k -dimensional faces.

We have applied the general theory to some prototypical examples. The first one is a set of manifolds described by ℓ_2 ellipsoids. These manifolds are analogous to a generative model consisting of a mixture of low-dimensional Gaussians, but with bounded extent so that the ellipsoids have zero overlap. These manifolds are strictly convex, and we show how the interior, touching, and fully embedded support regimes contribute to the overall capacity as a function of the principal radii of the ellipsoids.

We have also applied the theory to manifolds with non-smooth convex hulls. One example is ℓ_1 balls that exhibit a polytope geometry. The other example is orientation manifolds that are parameterized by a single angular variable. Because of the faceted nature of these convex hulls, the Gaussian random \vec{t} induces a distribution on embedding dimensions, k , of the support faces, reflecting an interesting signature of the geometry of the convex hull. Changing the overall size of the manifolds shifts the distribution of k towards higher values as the manifolds become increasingly embedded in the margin planes. Despite the qualitative differences in the underlying geometries of the two examples, both exhibit a weak, logarithmic growth of Gaussian dimension with the affine dimension, D , reflecting the large anisotropy in the shape of the convex hulls.

We have extended the theory for label imbalance, when the vast majority of the manifolds belong to a single class, which can be taken as $y^\mu = -1$ without loss of generality. In the extreme limit where only one manifold is positively labeled, the task is related to *object recognition* since the classifier is trained to indicate the presence of a single object. Combining sparse classifiers to solve multi-class recognition problems would be an interesting extension of the present work. We show that classification with sparse labels enjoy higher capacity, or larger margins at the same load, as compared to balanced classes. The enhanced capacity is particularly important for large and high dimensional manifolds, as their balanced capacity is quite small. Our analysis indeed reveals the important interplay between label sparsity and manifold geometry in determining the classification capacity.

We have elucidated the major effects of the geometrical properties of the manifold convex hulls on their classification capacity. However, to apply the theory quantitatively to experimental data, several outstanding issues need to be addressed, including:

Correlations: In the present work we have assumed that the directions of the affine subspaces of the different manifolds are uncorrelated. In realistic situations we expect to see correlations in the manifold geometries, mainly of two types: One is center-center correlations. Such correlations can be harmful for linear separability [32, 33]. Another is correlated variability in which the directions of the affine subspaces are correlated but not the centers. Positive correlations of the latter form are beneficial for separability. In the extreme case when the manifolds share a common affine subspace, the rank of the union of the subspaces is $D_{tot} = D$ rather than $D_{tot} = PD$, and the solution weight vector need only lie in the null space of this smaller subspace. Further work is needed to extend the present theory to incorporate more general correlations.

Generalization performance: We have studied the separability of manifolds with known geometries. In many realistic problems, this information is not readily available and only samples reflecting the natural variability of input patterns are provided. These samples can be used to estimate the underlying manifold model (using manifold learning techniques [34, 35]) and/or to train a classifier based upon a finite training set. Generalization error [36] describes how well a classifier trained on a finite number of samples would perform on other test points drawn from the manifolds. It would be important to extend our theory to calculate the expected generalization error achieved by the maximum margin solution trained on *point cloud manifolds*, as a function of the size of the training set and the geometry of the underlying full manifolds.

Unrealizable classification: Throughout the present work, we have assumed that the manifolds are sepa-

rable by a linear classifier. In realistic problems, the load may be above the capacity for linear separation, i.e. $\alpha > \alpha_M(\kappa = 0)$. Alternatively, neural noise may cause the manifolds to be unbounded in extent, with the tails of their distribution overlapping so that they are not separable with zero error. There are several ways to handle this issue in supervised learning problems. One possibility is to map the unrealizable representation nonlinearly to a higher dimensional feature space, via a multi-layer network or nonlinear kernel function, where the classification can be performed with zero error. The design of multilayer networks could be facilitated using manifold processing principles uncovered by our theory.

Another possibility is to introduce an optimization problem allowing a small training error, for example, using an SVM with complementary slack variables [14]. These procedures raise interesting theoretical challenges, including understanding how the geometry of manifolds change as they undergo nonlinear transformations, as well as investigating by statistical mechanics, the performance of a linear classifier of manifolds with slack variables [37].

Concluding remarks: The statistical mechanical theory of perceptron learning has long provided a basis for understanding the performance and fundamental limitations of single layer neural architectures and their kernel extensions. However, the previous theory only considered a finite number of random points with no underlying geometric structure, and could not explain the performance of linear classifiers on large, possibly infinite number of inputs organized as distinct manifolds by the variability due to changes in physical parameters of objects. The statistical mechanical theory presented in this work can explain the capacity and limitations of linear classification of general manifolds, and be used to elucidate changes in neural representations across hierarchical sensory systems. We believe the application of this theory and its corollary extensions will precipitate novel insights into how perceptual systems, biological or artificial, can efficiently code and process sensory information.

We would like to thank Uri Cohen, Ryan Adams, Leslie Valiant, David Cox, Jim DiCarlo, Doris Tsao, and Yoram Burak for helpful discussions. The work is partially supported by the Gatsby Charitable Foundation, the Swartz Foundation, the Simons Foundation (SCGB Grant No. 325207), the NIH, and the Human Frontier Science Program (Project RGP0015/2013). D. D. Lee also acknowledges the support of the US National Science Foundation, Army Research Laboratory, Office of Naval Research, Air Force Office of Scientific Research, and Department of Transportation.

APPENDIX A: REPLICA THEORY OF MANIFOLD CAPACITY

In this section, we outline the derivation of the mean field replica theory summarized in Eqs. (11)-(12). We define the capacity of linear classification of manifolds, $\alpha_M(\kappa)$, as the maximal load, $\alpha = \frac{P}{N}$, for which with high probability a solution to $y^\mu \mathbf{w} \cdot \mathbf{x}^\mu \geq \kappa$ exists for a given κ . Here \mathbf{x}^μ are points on the P manifolds M^μ , Eq. (1), and we assume that all $NP(D+1)$ components of $\{\mathbf{u}_i^\mu\}$ are drawn independently from a Gaussian distribution with zero mean and variance $\frac{1}{N}$, and that the binary labels $y^\mu = \pm 1$ are randomly assigned to each manifold with equal probabilities. We consider the thermodynamic limit where $N, P \rightarrow \infty$ but $\alpha = \frac{P}{N}$, and D are finite.

Note that the geometric margin, κ' , defined as the distance from the solution hyperplane is given by $y^\mu \mathbf{w} \cdot \mathbf{x}^\mu \geq \kappa' \|\mathbf{w}\| = \kappa' \sqrt{N}$. However, this distance depends on the scale of the input vectors \mathbf{x}^μ . The correct scaling of the margin in the thermodynamic limit is $\kappa' = \frac{\|\mathbf{x}\|}{\sqrt{N}} \kappa$. Since we adopted the normalization of $\|\mathbf{x}^\mu\| = O(1)$, the correct scaling of the margin is $y^\mu \mathbf{w} \cdot \mathbf{x}^\mu \geq \kappa$.

Evaluation of solution volume: Following Gardner's replica framework, we first consider the volume V of the solution space for $\alpha < \alpha_M(\kappa)$. We define the signed projections of the i th direction vector \mathbf{u}_i^μ on the solution weight as $h_i^\mu = \sqrt{N} y^\mu \mathbf{w} \cdot \mathbf{u}_i^\mu$, where $i = 1, \dots, D+1$ and $\mu = 1, \dots, P$. Then, the separability constraints can be written as $\sum_{i=1}^{D+1} s_i h_i^\mu \geq \kappa$. Hence the volume can be written as

$$V = \int d^N \mathbf{w} \delta(\mathbf{w}^2 - N) \prod_{\mu=1}^P \Theta_\mu \left(-g_S(-\vec{h}^\mu) - \kappa \right) \quad (\text{A.1})$$

where $\Theta(x)$ is a Heavyside step function. g_S is the support function of \mathcal{S} defined in Eq. (13) as $g_S(\vec{v}) = \max \{ \vec{v} \cdot \vec{s} \mid \vec{s} \in \mathcal{S} \}$.

The volume defined above depends on the quenched random variables \mathbf{u}_i^μ and y^μ through h_i^μ . It is well known that in order to obtain the typical behavior in the thermodynamic limit, we need to average $\log V$, which we carry out using the replica trick, $\langle \log V \rangle = \lim_{n \rightarrow 0} \frac{\langle V^n \rangle - 1}{n}$, where $\langle \rangle$ refers to the average over \mathbf{u}_i^μ and y^μ . For natural n , we need to evaluate,

$$\begin{aligned} \langle V^n \rangle &= \int \prod_{\alpha}^n d\mathbf{w}_\alpha \delta(\mathbf{w}_\alpha^2 - N) \prod_{\mu}^P \int \mathbb{D} \vec{h}^{\mu\alpha} \quad (\text{A.2}) \\ &\quad \left\langle \prod_i^{D+1} \sqrt{2\pi} \delta(h_i^{\mu\alpha} - y^\mu w_\alpha^T \mathbf{u}_i^\mu) \right\rangle_{\mathbf{u}_i^\mu, y^\mu} \end{aligned}$$

where we have used the notation,

$$\mathbb{D} \vec{h} = \prod_{i=1}^{D+1} \frac{dh_i}{\sqrt{2\pi}} \Theta \left(-g_S(-\vec{h}) - \kappa \right) \quad (\text{A.3})$$

Using Fourier representation of the delta functions, we obtain

$$\langle V^n \rangle = \int \prod_{\alpha}^n d\mathbf{w}_{\alpha} \delta(\mathbf{w}_{\alpha}^2 - N) \prod_{\mu}^P \int \mathbb{D}\vec{h}^{\mu\alpha} \quad (\text{A.4})$$

$$\prod_{i=1}^{D+1} \int \frac{d\hat{h}_i^{\mu\alpha}}{\sqrt{2\pi}} \left\langle \exp \left\{ i\hat{h}_i^{\mu\alpha} (h_i^{\mu\alpha} - y^{\mu} \mathbf{w}_{\alpha}^T \mathbf{u}_i^{\mu}) \right\} \right\rangle_{\mathbf{u}_i^{\mu}, y^{\mu}}$$

Performing the average over the Gaussian distribution of \mathbf{u}_i^{μ} (each of the N components has zero mean and variance $\frac{1}{N}$) yields,

$$\left\langle \exp \sum_{i=1}^{D+1} \sum_{\mu\alpha} \left[i\hat{h}_i^{\mu\alpha} (-y^{\mu} \sum_{j=1}^N w_{\alpha}^j \mathbf{u}_{i,j}^{\mu}) \right] \right\rangle_{\mathbf{u}_i^{\mu}, y^{\mu}} \quad (\text{A.5})$$

$$= \exp \left\{ -\frac{1}{2} \sum_{\alpha\beta} \mathbf{q}_{\alpha\beta} \sum_{i\mu} \hat{h}_i^{\mu\alpha} \hat{h}_i^{\mu\beta} \right\}$$

where, $\mathbf{q}_{\alpha\beta} = \frac{1}{N} \sum_{j=1}^N w_{\alpha}^j w_{\beta}^j$. Thus, integrating the variables $\hat{h}_i^{\mu\alpha}$ yields

$$\langle V^n \rangle = \int \prod_{\alpha=1}^n d\mathbf{w}_{\alpha} \delta(\mathbf{w}_{\alpha}^2 - N) \int d\mathbf{q}_{\alpha\beta} \Pi_{\alpha\beta} \quad (\text{A.6})$$

$$\cdot \delta(N\mathbf{q}_{\alpha\beta} - \mathbf{w}_{\alpha}^T \mathbf{w}_{\beta}) \left[\exp \left(-\frac{(D+1)}{2} \log \det \mathbf{q} \right) X \right]^P$$

where

$$X = \int \prod_{\alpha} \mathbb{D}\vec{h}^{\alpha} \exp \left[-\frac{1}{2} \sum_{i,\alpha,\beta} h_i^{\alpha} (\mathbf{q}^{-1})_{\alpha\beta} h_i^{\beta} \right] \quad (\text{A.7})$$

and we have used the fact that all manifolds contribute the same factor.

We proceed by making the replica symmetric ansatz on the order parameter $\mathbf{q}_{\alpha\beta}$ at its saddle point, $\mathbf{q}_{\alpha\beta} = (1-q)\delta_{\alpha\beta} + q$, from which one obtains in the $n \rightarrow 0$ limit:

$$\mathbf{q}_{\alpha\beta}^{-1} = \frac{1}{1-q} \delta_{\alpha\beta} - \frac{q}{(1-q)^2} \quad (\text{A.8})$$

and

$$\log \det \mathbf{q} = n \log(1-q) + \frac{nq}{1-q} \quad (\text{A.9})$$

Thus the exponential term in X can be written as

$$\exp \left[-\frac{1}{2} \sum_{\alpha i} \frac{(h_i^{\alpha})^2}{1-q} + \frac{1}{2} \sum_i \left(\frac{\sqrt{q}}{1-q} \sum_{\alpha} h_i^{\alpha} \right)^2 \right] \quad (\text{A.10})$$

Using the Hubbard–Stratonovich transformation, we obtain

$$X = \int D\vec{t} \left[\int \mathbb{D}\vec{h} \exp \left\{ -\frac{1}{2} \frac{\vec{h}^2}{1-q} + \frac{\sqrt{q}}{1-q} \vec{h} \cdot \vec{t} \right\} \right]^n \quad (\text{A.11})$$

where $D\vec{t} = \prod_i \frac{dt_i}{\sqrt{2\pi}} \exp \left(-\frac{t_i^2}{2} \right)$. Completing the square in the exponential and using $\int D\vec{t} A^n = \exp n \int D\vec{t} \log A$ in the $n \rightarrow 0$ limit, we obtain, $X = \exp \left(\frac{nq}{2(1-q)} + n \int D\vec{t} \log Z(\vec{t}) \right)$ with

$$Z(\vec{t}) = \int \mathbb{D}\vec{h} \exp \left\{ -\frac{1}{2(1-q)} \|\vec{h} - \sqrt{q}\vec{t}\|^2 \right\} \quad (\text{A.12})$$

Combining these terms, we write the last factor in Eq. (A.6) as $\exp nPG_1$ where,

$$G_1 = \int D\vec{t} \log Z(\vec{t}) - \frac{(D+1)}{2} \log(1-q) \quad (\text{A.13})$$

The first factors in $\langle V^n \rangle$, Eq. (A.6), can be written as $\exp nNG_0$, where as in the Gardner theory, the entropic term in the thermodynamic limit is

$$G_0(q) = \frac{1}{2} \ln(1-q) + \frac{q}{2(1-q)} \quad (\text{A.14})$$

and represents the constraints on the volume of \mathbf{w}_{α} due to normalization and the order parameter \mathbf{q} . Combining the G_0 and G_1 contributions, we have

$$\langle V^n \rangle_{t_0, t} = e^{Nn[G_0(q) + \alpha G_1(q)]} \quad (\text{A.15})$$

The classification constraints contribute αG_1 , with Eq. (A.13), and

$$Z(\vec{t}) = \int \prod_{i=1}^{D+1} \frac{dz_i}{\sqrt{2\pi(1-q)}} \exp \left(-\frac{\vec{z}^2}{2(1-q)} \right) \quad (\text{A.16})$$

$$\Theta(-g_S(-\sqrt{q}\vec{t} - \vec{z}) - \kappa)$$

where, we have written the fields h_i as

$$h_i = \sqrt{q}t_i + z_i \quad (\text{A.17})$$

Note that $\sqrt{q}t_i$ represents the quenched random component due to the randomness in the \mathbf{u}_i^{μ} , and z_i is the “thermal” component due to the variability within the solution space. The order parameter q is calculated via $0 = \frac{\partial G_0}{\partial q} + \alpha \frac{\partial G_1}{\partial q}$.

Capacity: In the limit where $\alpha \rightarrow \alpha_M(\kappa)$, the overlap between the solutions become unity and the volume shrinks to zero. It is convenient to define $Q = \frac{q}{1-q}$ and study the limit of $Q \rightarrow \infty$. In this limit the leading order is

$$\langle \log V \rangle = \frac{Q}{2} [1 - \alpha \langle F(\vec{t}) \rangle_{\vec{t}}] \quad (\text{A.18})$$

where the first term is the contribution from $G_0 \rightarrow \frac{Q}{2}$. The second term comes from $G_1 \rightarrow -\frac{Q}{2} \alpha \langle F(\vec{t}) \rangle_{\vec{t}}$, where

the average is over the Gaussian distribution of the $D+1$ dimensional vector \vec{t} , and

$$F(\vec{t}) \rightarrow -\frac{2}{Q} \log Z(\vec{t}) \quad (\text{A.19})$$

is independent of Q and is given by replacing the integrals in Eq. (A.16) by their saddle point, which yields

$$F(\vec{t}) = \min_{\vec{z}} \left\{ \|\vec{z}\|^2 \mid g_S(-\vec{t} - \vec{z}) + \kappa \leq 0 \right\} \quad (\text{A.20})$$

It is convenient to change variables by introducing $\vec{v} = -\vec{t} - \vec{z}$, and write $F(\vec{t}) = \min_{\vec{v}} \left\{ \|\vec{v} + \vec{t}\|^2 \mid g_S(\vec{v}) + \kappa \leq 0 \right\}$. Noting that the distribution of \vec{t} is invariant under $\vec{t} \rightarrow -\vec{t}$, we obtain the final form, $F(\vec{t}) = \min_{\vec{v}} \left\{ \|\vec{v} - \vec{t}\|^2 \mid g_S(\vec{v}) + \kappa \leq 0 \right\}$. At the capacity, $\log V$ vanishes, the capacity of a general manifold with margin κ , is given by,

$$\alpha_M^{-1}(\kappa) = \langle F(\vec{t}) \rangle_{\vec{t}} \quad (\text{A.21})$$

$$F(\vec{t}) = \min_{\vec{v}} \left\{ \|\vec{v} - \vec{t}\|^2 \mid g_S(\vec{v}) + \kappa \leq 0 \right\} \quad (\text{A.22})$$

Finally, we note that the mean squared 'annealed' variability in the fields due to the entropy of solutions vanishes at the capacity limit, as $1/Q$, see Eq. (A.16). Thus, the quantity $\|\vec{v} - \vec{t}\|^2$ in the above equation represents the annealed variability times Q which remains finite in the limit of $Q \rightarrow \infty$.

APPENDIX B: CAPACITY OF ℓ_2 BALLS WITH SPARSE LABELS

Here we outline the mean field theory of the capacity of sparsely labeled ℓ_2 balls. The capacity of balls with balanced labels (and zero bias) is

$$\begin{aligned} \alpha_B^{-1} &= \int_0^\infty dt \chi_D(t) \int_{-\kappa-rt}^{-\kappa+tr^{-1}} Dt_0 \frac{(t_0 + tr + \kappa)^2}{(1+r^2)} \\ &+ \int_0^\infty dt \chi_D(t) \int_{-\kappa+tr^{-1}}^\infty Dt_0 [(t_0 + \kappa)^2 + t^2] \end{aligned} \quad (\text{A.23})$$

where,

$$\chi_D(t) = \frac{2^{1-\frac{D}{2}}}{\Gamma(\frac{D}{2})} t^{D-1} e^{-\frac{1}{2}t^2}, \quad t \geq 0 \quad (\text{A.24})$$

is the D -dimensional Chi probability density function. Eq. (71) then yields,

$$\begin{aligned} \alpha_B^{-1} &= f \int_0^\infty dt \chi_D(t) \\ &\left[\int_{-b-\kappa-tr}^{-b-\kappa+tr^{-1}} Dt_0 \frac{(t_0 + tr + b + \kappa)^2}{(1+r^2)} \right. \\ &\quad \left. + \int_{-b-\kappa+tr^{-1}}^\infty Dt_0 ((t_0 + b + \kappa)^2 + t^2) \right] \\ &+ (1-f) \int_0^\infty dt \chi_D(t) \\ &\left[\int_{b-\kappa-tr}^{b-\kappa+rt^{-1}} Dt_0 \frac{(t_0 + tr - b + \kappa)^2}{(1+r^2)} \right. \\ &\quad \left. + \int_{b-\kappa+tr^{-1}}^\infty Dt_0 ((t_0 - b + \kappa)^2 + t^2) \right] \end{aligned} \quad (\text{A.25})$$

and the optimal bias b is given by $\partial \alpha_B / \partial b = 0$.

Small r : First, we note that the capacity of sparsely labeled points is $\alpha_0(f, \kappa) = \max_b \alpha_0(f, \kappa, b)$, where

$$\begin{aligned} \alpha_0^{-1}(f, \kappa, b) &= f \int_{-b-\kappa}^\infty Dt(t - \kappa - b)^2 \\ &+ (1-f) \int_{b-\kappa}^\infty Dt(t - \kappa + b)^2 \end{aligned} \quad (\text{A.26})$$

and optimizing b yields the following equation for b ,

$$0 = f \int_{-b-\kappa}^\infty Dt(t - \kappa - b) + (1-f) \int_{b-\kappa}^\infty Dt(t - \kappa + b) \quad (\text{A.27})$$

Next, for balls with small radius, such that $r\sqrt{D} \lesssim 1$, we can use the general theory of manifolds in the scaling regime, Sec. V, which predicts that,

$$\alpha_B(f, R, D) \approx \alpha_0(f, \kappa = r\sqrt{D}) \quad (\text{A.28})$$

Small f and large r : Here we analyze the above equations in the limit of small f and large r . We assume that f is sufficiently small so that the optimal bias b is large. Furthermore, since r is large, in order to be effective, b must be of the order of r or larger. Hence we assume that the scaled bias, $\bar{b} = \frac{b}{\sqrt{1+R^2}}$, is order 1 or larger. Under these conditions, the contribution of the minority class to the inverse capacity α_B^{-1} is dominated by

$$f \int_0^\infty dt \chi_D(t) \int_{-b+tr^{-1}}^\infty Dt_0 ((t_0 + b)^2 + t^2) \approx fb^2 \quad (\text{A.29})$$

where we have assumed $\kappa = 0$ for simplicity. The dominant contribution of the majority class to α_B^{-1} is,

$$(1-f) \int_0^\infty dt \chi_D(t) \int_{b-tr}^{b+rt^{-1}} Dt_0 \frac{(t_0 + tr - b)^2}{(1+r^2)} \quad (\text{A.30})$$

$$\approx (1-f) \int_{\bar{b}}^\infty dt \chi_D(t) (t - \bar{b})^2 \quad (\text{A.31})$$

In deriving the last equation we used $\frac{(t_0+tr-b)^2}{(1+r^2)} \rightarrow (t-\bar{b})^2$ as $r, b \rightarrow \infty$. Second, the integrals are of substantial value only if $t \geq \bar{b}$ in which case the integral of t_0 is $\int_{-r(\bar{b}-t)}^b Dt_0 \approx 1$ and the integral over t is from \bar{b} to ∞ . Combining the two results yields Eq. (75).

-
- [1] J. J. DiCarlo and D. D. Cox, Trends in cognitive sciences **11**, 333 (2007).
 - [2] J. K. Bizley and Y. E. Cohen, Nature Reviews Neuroscience **14**, 693 (2013).
 - [3] K. A. Bolding and K. M. Franks, eLife **6**, e22630 (2017).
 - [4] H. S. Seung and D. D. Lee, Science **290**, 2268 (2000).
 - [5] J. J. DiCarlo, D. Zoccolan, and N. C. Rust, Neuron **73**, 415 (2012).
 - [6] B. Poole, S. Lahiri, M. Raghu, J. Sohl-Dickstein, and S. Ganguli, in *Advances In Neural Information Processing Systems* (2016) pp. 3360–3368.
 - [7] M. A. Ranzato, F. J. Huang, Y.-L. Boureau, and Y. LeCun, in *Computer Vision and Pattern Recognition, 2007. CVPR'07. IEEE Conference on* (IEEE, 2007) pp. 1–8.
 - [8] Y. Bengio, Foundations and trends® in Machine Learning **2**, 1 (2009).
 - [9] I. Goodfellow, H. Lee, Q. V. Le, A. Saxe, and A. Y. Ng, in *Advances in neural information processing systems* (2009) pp. 646–654.
 - [10] C. F. Cadieu, H. Hong, D. L. Yamins, N. Pinto, D. Ardila, E. A. Solomon, N. J. Majaj, and J. J. DiCarlo, PLoS Comput Biol **10**, e1003963 (2014).
 - [11] T. M. Cover, IEEE transactions on electronic computers , 326 (1965).
 - [12] E. Gardner, Journal of physics A: Mathematical and general **21**, 257 (1988).
 - [13] E. Gardner, EPL (Europhysics Letters) **4**, 481 (1987).
 - [14] V. Vapnik, *Statistical learning theory* (Wiley New York, 1998).
 - [15] S. Chung, D. D. Lee, and H. Sompolinsky, Physical Review E **93**, 060301 (2016).
 - [16] S. Boyd and L. Vandenberghe, *Convex optimization* (Cambridge university press, 2004).
 - [17] R. T. Rockafellar, *Convex analysis* (Princeton university press, 2015).
 - [18] J.-J. Moreau, CR Acad. Sci. Paris **225**, 238 (1962).
 - [19] S. Chung, U. Cohen, H. Sompolinsky, and D. D. Lee, arXiv preprint arXiv:1705.09944 (2017).
 - [20] B. Grünbaum and G. C. Shephard, Bulletin of the London Mathematical Society **1**, 257 (1969).
 - [21] R. Vershynin, in *Sampling theory, a renaissance* (Springer, 2015) pp. 3–66.
 - [22] A. Giannopoulos, V. Milman, and M. Rudelson, in *Geometric aspects of functional analysis* (Springer, 2000) pp. 81–93.
 - [23] K. Rajan, L. Abbott, and H. Sompolinsky, Physical Review E **82**, 011903 (2010).
 - [24] A. Litwin-Kumar, K. D. Harris, R. Axel, H. Sompolinsky, and L. Abbott, Neuron **93**, 1153 (2017).
 - [25] J. Deng, W. Dong, R. Socher, L.-J. Li, K. Li, and L. Fei-Fei, in *Computer Vision and Pattern Recognition, 2009. CVPR 2009. IEEE Conference on* (IEEE, 2009) pp. 248–255.
 - [26] C. Szegedy, W. Liu, Y. Jia, P. Sermanet, S. Reed, D. Anguelov, D. Erhan, V. Vanhoucke, and A. Rabinovich, in *Proceedings of the IEEE Conference on Computer Vision and Pattern Recognition* (2015) pp. 1–9.
 - [27] M. B. McCoy and J. A. Tropp, Discrete & Computational Geometry **51**, 926 (2014).
 - [28] S.-H. Kye, arXiv preprint arXiv:1302.2226 (2013).
 - [29] Z. Smilansky, Israel Journal of Mathematics **52**, 115 (1985).
 - [30] H. S. Seung and H. Sompolinsky, Proceedings of the National Academy of Sciences **90**, 10749 (1993).
 - [31] P. Gao and S. Ganguli, Current opinion in neurobiology **32**, 148 (2015).
 - [32] R. Monasson, Journal of Physics A: Mathematical and General **25**, 3701 (1992).
 - [33] B. Lopez, M. Schroder, and M. Opper, Journal of Physics A: Mathematical and General **28**, L447 (1995).
 - [34] S. T. Roweis and L. K. Saul, Science **290**, 2323 (2000).
 - [35] J. B. Tenenbaum, V. De Silva, and J. C. Langford, science **290**, 2319 (2000).
 - [36] S.-i. Amari, N. Fujita, and S. Shinomoto, Neural Computation **4**, 605 (1992).
 - [37] S. Risau-Gusman and M. B. Gordon, Physical Review E **64**, 031907 (2001).